Available online at www.sciencedirect.com
ScienceDirect
Journal of Sound and Vibration 324 (2009) 861–891
JOURNAL OF SOUND AND VIBRATION
www.elsevier.com/locate/jsvi

Broadband shock-cell noise from dual stream jets

Christopher K.W. Tam[a,*], N.N. Pastouchenko[a], K. Viswanathan[b]

[a]*Department of Mathematics, Florida State University, Tallahassee, FL 32306-4510, USA*
[b]*The Boeing Company, Seattle, WA 98124, USA*

Received 19 September 2008; received in revised form 11 February 2009; accepted 12 February 2009
Handling Editor: P. Joseph
Available online 18 March 2009

Abstract

Broadband shock-cell noise from dual stream jets is investigated. The present work is confined to the cases of supersonic secondary jet and subsonic primary jet. Previous studies on single stream supersonic jets reveal that broadband shock-cell noise from these jets is generated by the interaction of the large turbulence structures and the shock cells in the jet plume as the former propagate downstream through the latter. A prominent characteristic of the radiated noise is that it is most intense in the upstream direction and drops off with an increase in inlet angle. An important result of the present investigation is the discovery that there are two sets of broadband shock-cell noise. One set is the classical shock-cell noise, similar to that of single stream jets. The second set radiates sound primarily in the downstream direction. Its intensity is low at 90°, but the intensity increases with inlet angle until a critical angle is reached beyond which it starts to decrease rapidly. It is believed that the first sound field is generated by the interaction of the large turbulence structures and the shock cells in the outer shear layer of the dual stream jet. The second sound field is generated in a similar manner involving the large turbulence structures and the shock cells in the inner shear layer of the jet. The inner shear layer separates the secondary and the primary jet. A simplified mathematical model capable of elucidating the generation, transmission and radiation of broadband shock-cell noise from dual stream jets is developed. The model provides formulas relating the direction of radiation and the frequencies of broadband shock-cell noise at the peaks of the noise spectra for both sets of sound fields. Good agreement is found between the predictions from these formulas and experimental measurements, thereby providing support for the validity of the model.

1. Introduction

Broadband shock-cell noise associated with dual stream jets is investigated theoretically and experimentally. During certain cruise segments, the turbofan engines operate with a supersonic secondary stream and a subsonic primary stream; the temperature of the secondary stream is slightly elevated above ambient values, while the primary stream is heated. This typical jet operating condition is investigated in the present study. The engine noise, which consists of both shock-cell and turbulent mixing noise, impinge on the aircraft fuselage and is then transmitted inside. In the aft-cabin, the engine noise is an important component

*Corresponding author. Tel.: +1 850 644 2455; fax: +1 850 644 4053.
E-mail address: tam@math.fsu.edu (C.K.W. Tam).

0022-460X/$ - see front matter © 2009 Elsevier Ltd. All rights reserved.
doi:10.1016/j.jsv.2009.02.012

of cabin noise. The objectives of this work are two-fold: the first is to identify the salient characteristics of broadband shock-cell noise from dual stream jets and the second objective is to obtain an understanding of the noise generation mechanisms and the radiation properties through the development of a simple model. The validity of the model is tested by comparing its predictions with experimental measurements.

Most of the past efforts on broadband shock-cell noise research concentrated on single stream jets. Harper-Bourne and Fisher [1] were the first to identify broadband shock-cell noise as an important noise component of supersonic jets. Since their pioneering work, there have been a substantial number of experimental [2–14] and theoretical [15–18] studies of this noise component. Recent advances in computational aeroacoustics (CAA) provided a useful tool to investigate this noise component computationally [19–21]. All these research works concentrated on investigating the salient features and characteristics of broadband shock-cell noise, including spectral shape, directivity, noise generation mechanisms, and effects due to jet temperature and forward flight. Scaling formulas and semi-empirical prediction methods have also been developed. By-and-large, community noise was the prime motivation of the studies referenced above. More recent interest in shock-cell noise is associated with its role as a component of cabin noise at cruise. This shifts the attention to the noise from dual stream jets. There are now a number of investigations devoted to broadband shock-cell noise from dual stream jets [22–26]. These studies focus on the basic issues related to the shock-cell structure and the noise characteristics. Modification to the noise due to geometric modifications to the nozzle trailing edge has also been the subject of recent studies [27–29].

Past investigations on broadband shock-cell noise from single stream jets suggest that the noise is generated by the interaction of the large turbulence structures of the jet flow and the shock cells as the former propagate downstream through the latter. The large turbulence structures are coherent over a significant distance in the jet flow direction. Meanwhile, the shock-cell structure is spatially quasi-periodic. The shock-cell structure can, therefore, be decomposed into Fourier modes [26,30–32]. The Fourier modes are not exactly harmonics of each other as in the case of a perfectly periodic structure. The interaction between the large turbulence structures and each Fourier mode of the shock-cell structure leads to intense coherent noise radiation. The radiation is highly directional. Because there are a number of Fourier modes with significant amplitudes, the observed shock-cell noise spectrum often exhibits more than one peak. Each peak represents the noise generated by the interaction of the large turbulence structures and a single Fourier mode of the shock-cells. The dominant peak is, invariably, generated by the fundamental or the first Fourier mode of the shock-cells.

Fig. 1 shows the shock-cell noise spectra of a single stream Mach 1.67 cold jet measured by Norum and Seiner [7]. Seven spectra at 15° intervals are shown; the angles are measured from the jet inlet. The nozzle used in the experiment is a contoured convergent nozzle with an exit diameter of 3.982 cm. The spectra are measured by a microphone array at a distance of 3.05 m from the nozzle exit. Each noise spectrum is dominated by a single peak, the fundamental peak. A second peak can also be identified in the 75° and 90° spectra. Some of the principal characteristics of these spectra will now be briefly summarized. They are to be compared with the broadband shock-cell noise characteristic of dual stream jets in a later section.

First and foremost, the frequency at the peak of the broadband shock-cell noise spectrum (referred to as peak frequency) increases with direction of radiation (see Fig. 1). For instance, at 30° the peak frequency is around 2.5 kHz; at 120° it is 11 kHz. The fact that peak frequency is a strong function of direction of radiation suggests that noise radiation is coherent and directional and that it is from a coherent source. Another characteristic of broadband shock-cell noise is that the half-width of the spectral peak increases with the angle of radiation. At small inlet angles, the shock-cell noise spectrum has a very narrow peak. The half-width becomes quite broad at large inlet angles. Fig. 2 shows the directivity of broadband shock-cell noise for the same jet as in Fig. 1. The maximum levels of the noise spectra are plotted in this figure. It is clear that broadband shock-cell noise is radiated principally in the forward direction for a single stream jet and the noise level decreases rapidly with increase in inlet angle.

Earlier, Tam and Tanna [6] used a simple model to investigate how the interaction of large turbulence structures of the jet flow and a single Fourier mode of the shock-cell structure could lead to intense directional noise radiation. They modeled the large turbulence structures as traveling instability waves (Kelvin–Helmholtz

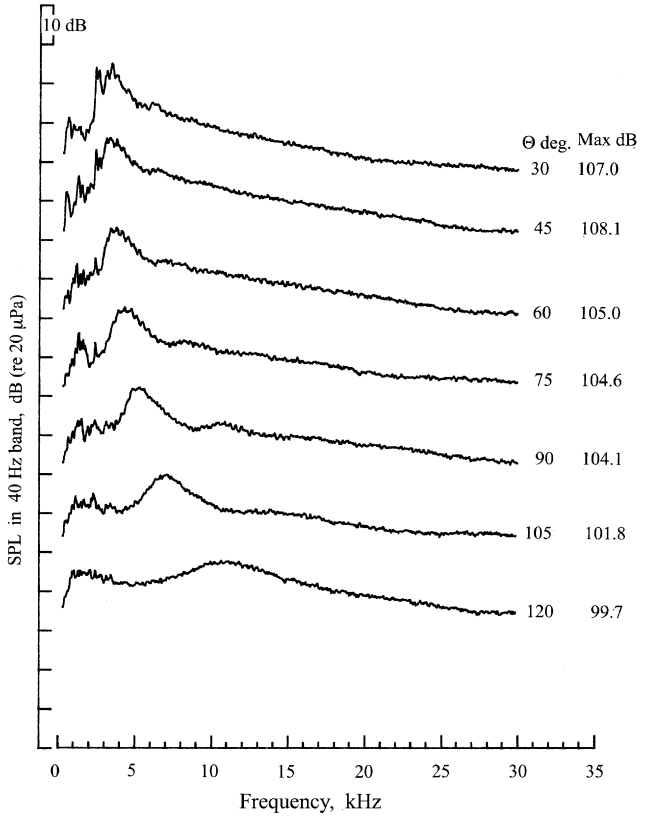

Fig. 1. Broadband shock-cell noise spectra of a single stream Mach 1.67 cold jet measured by Norum and Seiner [7].

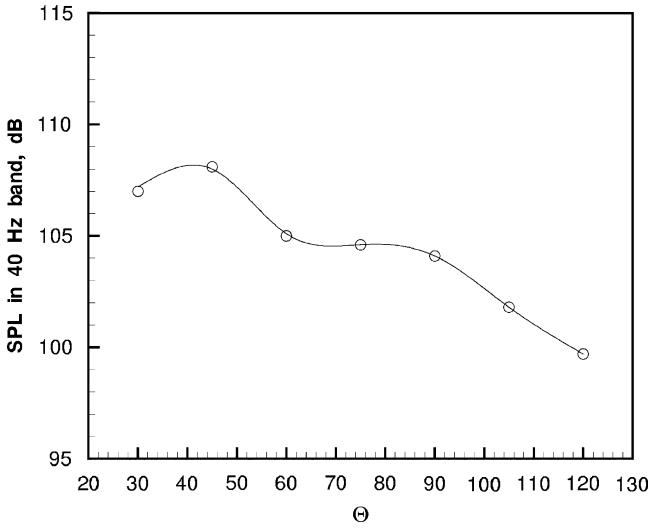

Fig. 2. Variation of maximum sound–pressure-level of broadband shock-cell noise with direction of radiation for the Mach 1.67 jet of Norum and Seiner [7].

instability). That is, the unsteady velocity of the large turbulence structures at an angular frequency ω and wavenumber k is represented by

$$u = \mathrm{Re}[a(x)\psi(r)\mathrm{e}^{\mathrm{i}(kx-\omega t)}] \tag{1}$$

where Re[ ] is the real part of [ ]. $a(x)$ is the amplitude of the instability wave and $\psi(r)$ the distribution of fluctuation in the radial direction. The convection velocity u_c of the wave is

$$u_c = \frac{\omega}{k}. \tag{2}$$

For the jth Fourier mode of the shock cells, Tam and Tanna chose to represent the velocity distribution by a cosine function in the form

$$u = A_j \phi_j(r) \cos(\alpha_j x) \tag{3}$$

where A_j and $\phi_j(r)$ are the amplitude and mode profile in the radial direction of the jth Fourier mode. α_j is the wavenumber. Now nonlinear interaction between instability wave/large turbulence structures and the jth shock-cell mode gives rise to disturbances involving product of the terms on the right sides of Eqs. (1) and (3). That is

$$\mathrm{Re}\left\{\frac{1}{2} a(x)\psi(r)A_j\phi_j(r)[e^{i(k+\alpha_j)x-i\omega t} + e^{i(k-\alpha_j)x-i\omega t}]\right\}. \tag{4}$$

The phase velocity of the second term of Eq. (4) is $\omega/(k–\alpha_j)$. If k is nearly equal to α_j, then the wave is supersonic; i.e., $|\omega/(k–\alpha_j)| > a_\infty$ where a_∞ is the ambient speed of sound. This will lead to Mach wave radiation as shown in Fig. 3. Suppose ϕ is the direction of Mach wave radiation, the Mach angle relationship gives

$$a_\infty = \frac{\omega}{k - \alpha_j} \cos\,\phi. \tag{5}$$

On using Eq. (2) to eliminate k, Eq. (5) may be rewritten in the form

$$f_j = \frac{\alpha_j u_c}{2\pi(1 + M_c \cos\,\Theta)} \tag{6}$$

where $\Theta = \pi - \phi$ is the inlet angle, f_j is the jth peak frequency of the broadband shock-cell noise spectrum ($f = \omega/2\pi$). $M_c = u_c/a_\infty$ is the convective Mach number of the large turbulence structures. Tam and Tanna demonstrated that Eq. (6) provided a good correlation of the peak frequency and direction of radiation for broadband shock-cell noise from single stream supersonic jets.

In this paper, we will show that unlike single stream supersonic jets, a dual stream jet radiates two components of broadband shock-cell noise. This finding is new. The origin of the second component of broadband shock-cell noise has not been discussed before in the literature. Section 2 of this paper describes briefly the experimental facility used in the noise measurements of the present investigation. In Section 3, experimental evidence will be offered to show the existence of two distinct components of broadband

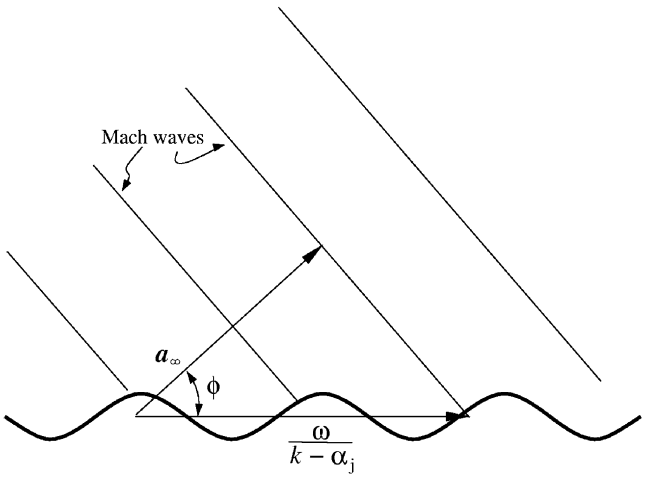

Fig. 3. Geometry of Mach wave radiation generated by a supersonic traveling wave.

shock-cell noise; their far-field characteristics will be examined. In Section 4 a simple vortex sheet jet model is used to show the generation, transmission, and radiation of the two components of broadband shock-cell noise. Comparisons of the predictions of the vortex sheet jet model and experimental measurements are given in Section 5. Section 6 provides a brief summary and the conclusions from this work.

2. Experimental program

The experiments of this investigation have been performed in the Low Speed Aeroacoustic Facility (LSAF) at Boeing. Detailed descriptions of the test facility, the jet simulator, the data acquisition and reduction process, etc. may be found in Viswanathan [33,34]. Fig. 4 shows a picture of the anechoic chamber, the jet simulator, the wind tunnel, and some of the microphones. The jet simulator is embedded in an open jet wind tunnel, which can provide a maximum free-stream Mach number of 0.32. The microphones are laid out at a constant sideline distance of 15 ft (4.572 m) from the jet axis, except the microphone at 155°, which is at a distance of 12.75 ft (3.886 m). All angles are measured from the jet inlet axis, with a polar angular range of 50°–155°. Additional microphones are also located at several polar angles at different azimuthal angles. Bruel & Kjaer Type 4939 quarter inch microphones are used for free-field measurements. The microphones are set at normal incidence and without the protective grid, which yields a flat frequency response up to 100 KHz. Narrowband data with a bin spacing of 23.4 Hz are acquired. All the static data have been corrected to a polar arc of 20 feet (6.096 m) from the center of the nozzle exit (coordinate system with origin at the center of the nozzle exit) and lossless conditions for storage. For convenience, the data are scaled to a distance of 100 primary jet diameters for presentation. The atmospheric attenuation is calculated using the method of Shields and Bass [35].

The area ratio of the nozzle selected for this study is 3.0, which is representative of the area ratio of the larger jet engines in service. The area of the primary nozzle is 4.714 in^2 (0.00304 m^2) and that of the secondary nozzle is 14.143 in^2 (0.00912 m^2). The primary nozzle extends beyond the secondary nozzle and the geometry is again typical of existing configurations. Fig. 5 shows a schematic diagram of the cross-section of the nozzle. The various dimensions are

$$H = 3\,\text{in}\ (7.62\,\text{cm}),\ W = 5.68\,\text{in}\ (14.42\,\text{cm}),\ D_p = 2.45\,\text{in}\ (6.22\,\text{cm}),\ h = 0.879\,\text{in}\ (2.23\,\text{cm}),\ \alpha = 8.95^\circ$$

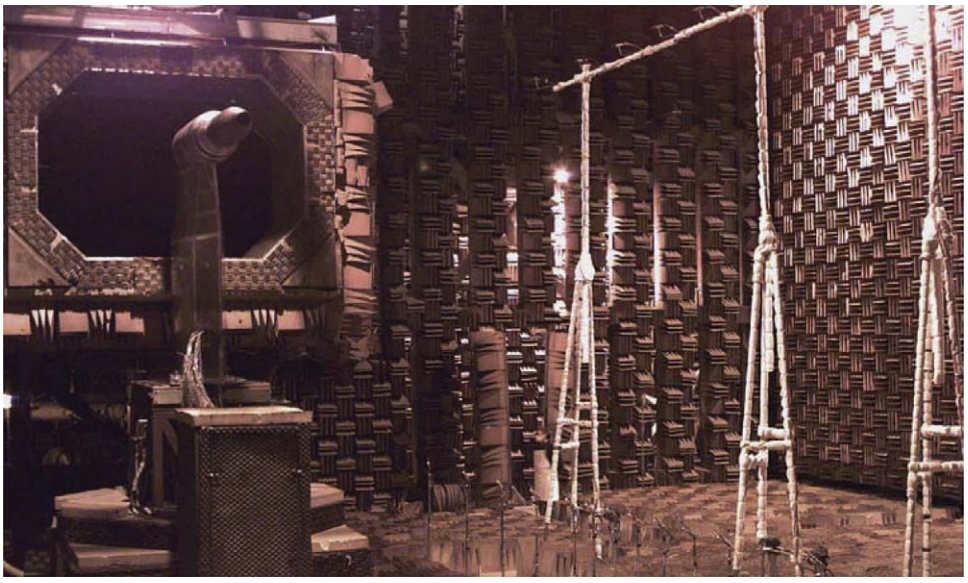

Fig. 4. Picture of the Low Speed Aeroacoustic Facility (LSAF) at the Boeing Company. Also shown are the jet simulator and microphone array.

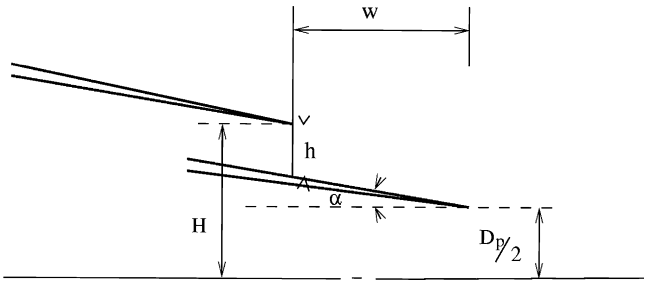

Fig. 5. Schematic diagram of the cross-section of a dual stream nozzle used in the present experiment.

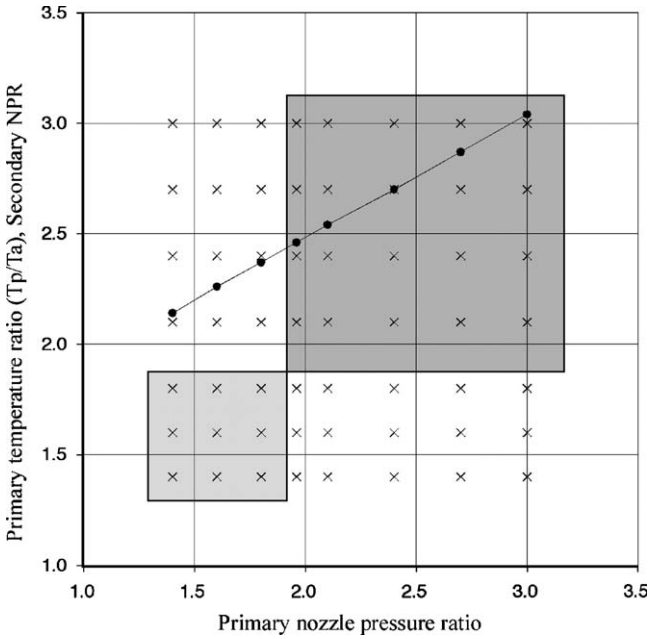

Fig. 6. Test matrix. Black dots are test points of the primary jet.

Since the main goal of this study is to enhance our understanding of the physical mechanisms, clean internal lines without struts, bifurcations, etc., are maintained so as to avoid complexities associated with asymmetries and other effects. Once the geometry is fixed, there are four thermodynamic variables, viz., the total pressures and temperatures in the two streams that may be varied independently. However, in order to keep the text matrix reasonably small, the temperature of the secondary stream is always maintained at ambient temperature. The value of the secondary temperature ratio ($T_s^{(r)}/T_a$, where $T_s^{(r)}$ denotes total temperature of the secondary jet, T_a denotes the ambient gas temperature) for most engines is ~1.15. Hence, the above choice is not too restrictive. When tests are carried out for actual engine geometries, the thermodynamic variables are set so as to match a given engine cycle. In order to ensure practical relevance, a typical engine cycle that has a fixed total temperature for a specified NPR is chosen for the primary stream. The NPR of the primary stream spans a range of 1.4–3.0, with a corresponding temperature ratio range ($T_p^{(r)}/T_a$, where $T_p^{(r)}$ is the total temperature of the primary jet) of 2.14–3.04. At every cycle point for the primary flow, the NPR in the secondary stream is systematically varied over a range of 1.4–3.0. The basic test matrix is shown in Fig. 6. The dark circles and the line define the test points of the primary jet, namely NPR_p and (T_p/T_a). The crosses denote the NPR in the secondary stream. Thus, an extensive database has been generated to provide high-quality data for the development and improvement of prediction methods for jet noise. The salient experimental results from this test matrix may be found in Viswanathan [36].

3. Observation of two components of broadband shock-cell noise from dual stream jets

There are many similarities between the broadband shock-cell noise of dual stream jets and single stream jets. However, there are also significant differences. One of the most important differences is that dual stream jets radiate two sets of broadband shock-cell noise. Experimental evidence will now be presented to support this observation. Fig. 7 shows the broadband shock-cell noise spectra of a dual stream jet with M_s (secondary jet Mach number) $= 1.36$, $T_s^{(r)}/T_a = 1.0$, M_p (primary jet Mach number) $= 0.72$ and $T_p^{(r)}/T_a = 2.14$. Nine spectra beginning with inlet angle 50° to inlet angle 130° at 10° interval are shown. The spectra at 50°–80° contain a prominent peak. This is the principal broadband shock-cell noise peak analogous to that of Fig. 1 for single stream jets. We will now confine our attention to the principal peak of the noise spectrum. The frequency of the spectral peak, indicated by a small black arrow, increases with the direction of radiation. This is the first component of broadband shock-cell noise from a dual stream jet. It has characteristics very similar to those of single stream supersonic jets. In Fig. 7, the noise spectrum at 90° shows two principal peaks. They overlap each other somewhat. For clarity, a small open arrow has been added to indicate the second peak. The existence of two peaks can be seen in the spectrum at 100°. These peaks appear to be natural continuation of those at 90°. At inlet angle larger than 100°, the maximum level of the first peak appears to be severely reduced. It is no longer readily observable at 110°. In contrast, the level of second peak increases and peaks at 110°. Beyond 110° the peak level decreases with increase in inlet angle. This peak remains observable in the noise spectrum at 130°.

Fig. 8 shows the noise spectra of a dual stream jet at $M_s = 1.36$, $T_s^{(r)}/T_a = 1.0$, $M_p = 0.85$, and $T_p^{(r)}/T_a = 2.26$. The shapes of the spectra are very similar to those of Fig. 7. Again, two sets of principal spectral peaks can be easily identified. Fig. 9 shows the noise spectra of another dual stream jet with $M_s = 1.28$, $T_s^{(r)}/T_a = 1.0$, $M_p = 0.85$, $T_p^{(r)}/T_a = 2.26$. In this figure, the Strouhal number is used and the figure is plotted in a log scale. Again, the spectra in this figure show two sets of broadband shock-cell noise confirming the observations of the previous two figures. It is easy to note that for the first broadband

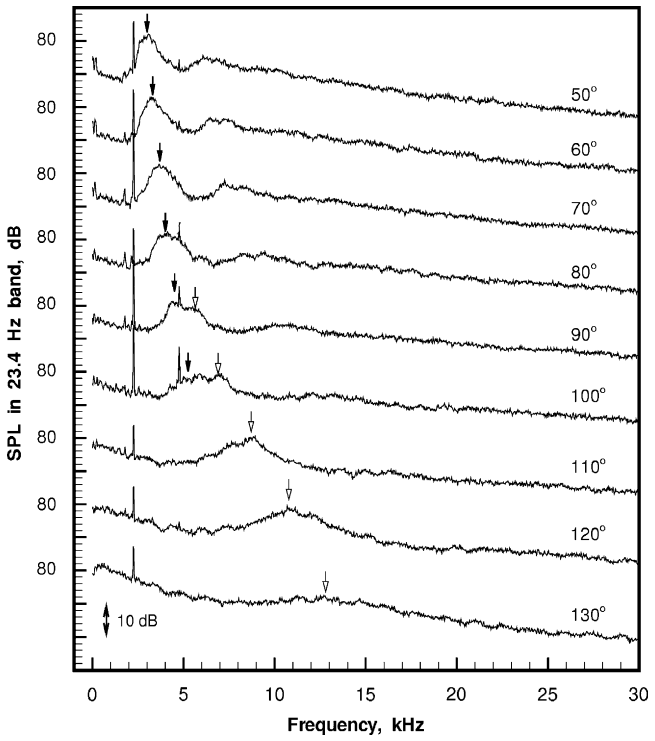

Fig. 7. Noise spectra of a dual stream jet at 10° interval. $M_p = 0.72$, $T_p^{(r)}/T_a = 2.14$, $M_s = 1.36$, $T_s^{(r)}/T_a = 1.0$. Black arrows indicate the first component of broadband shock-cell noise. Open arrows indicate the second component.

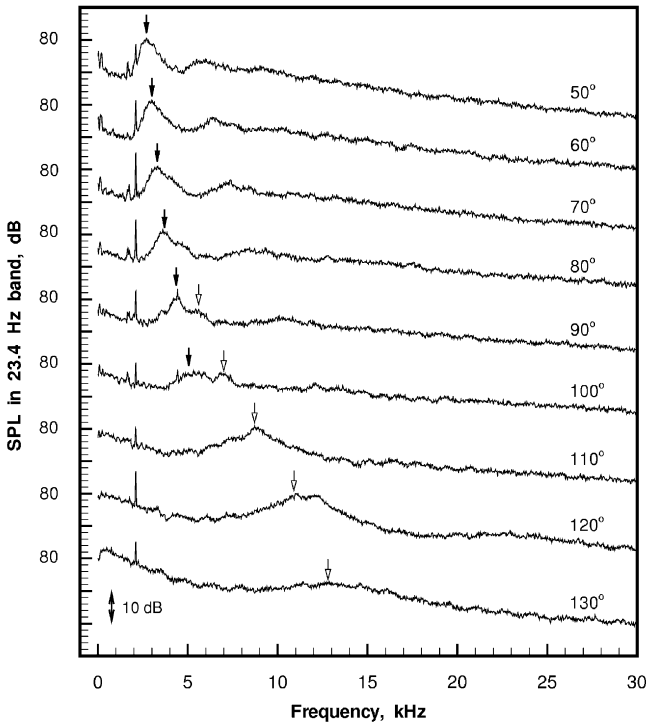

Fig. 8. Noise spectra of a dual stream jet at $M_p = 0.85$, $T_p^{(r)}/T_a = 2.26$, $M_s = 1.36$, $T_s^{(r)}/T_a = 1.0$.

shock-cell noise component in Figs. 6–8, the half-width of the spectral peak increases with increase in inlet angle. This property is the same as that of single stream jets. The second shock-cell noise component becomes clearly identifiable at 90° inlet angle. At this angle, the half-width of the spectral peak is relatively narrow. As inlet angle increases, the spectral half-width increases rapidly: a characteristic property of broadband shock-cell noise.

Another way to show that there are, indeed, two components of broadband shock-cell noise from dual stream jets is to examine the directivity of the maximum level of the observed spectral peaks. Fig. 10 shows the directivity of the $M_s = 1.36$, $T_s^{(r)}/T_a = 1.0$, $M_p = 0.72$, $T_p^{(r)}/T_a = 2.14$ jet. The maximum levels of the first two peaks of the first broadband shock-cell noise component from inlet angle 50°–100° are plotted. The directivity decreases with increase in inlet angle in much the same way as those of single jets (see Fig. 2). Starting from 90°, the directivity of the second broadband shock-cell noise component is plotted also in Fig. 10. The peak noise level increases and attains a maximum between 110° and 120°, beyond which the noise level drops rapidly. Clearly, the directivity plot of Fig. 10 is very different from Fig. 2, which shows the directivity for a single stream jet. Fig. 11 shows a similar directivity plot for the dual stream jet of Fig. 8. In this case, the intensity of the second shock-cell noise component rises to a level comparable to that of the first component. The directivity of the second shock-cell noise component shown in Figs. 10 and 11 is clearly different from the first component and that of single stream jets.

4. Noise generation, transmission, and radiation: a simplified model

4.1. Noise source model

The flow field and the shock-cell structure of a modern day dual stream commercial jet engine are fairly complex. Fig. 12 is a schematic diagram showing the most important features of the jet plume. There are two turbulent shear layers. The outer shear layer is formed by the mixing of the gas of the secondary jet and ambient air. The inner shear layer is formed by the mixing of the gases of the primary and secondary jets.

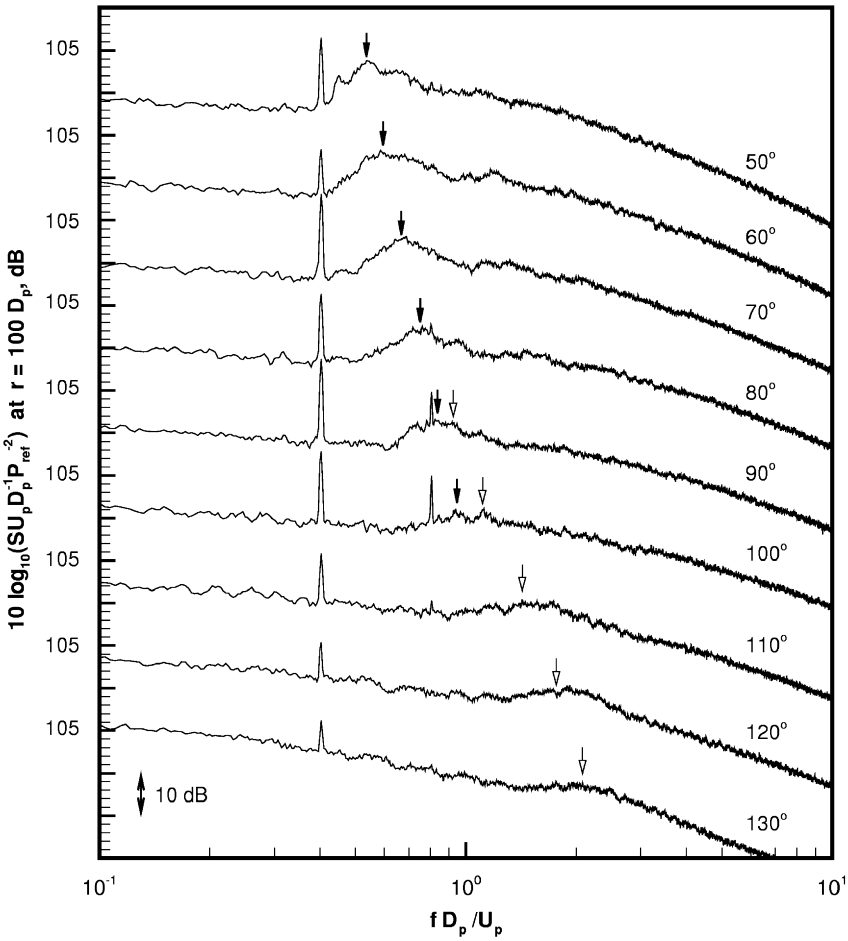

Fig. 9. Noise spectra of a dual stream jet at $M_p = 0.85$, $T_p^{(r)}/T_a = 2.26$, $M_s = 1.28$, $T_s^{(r)}/T_a = 1.0$.

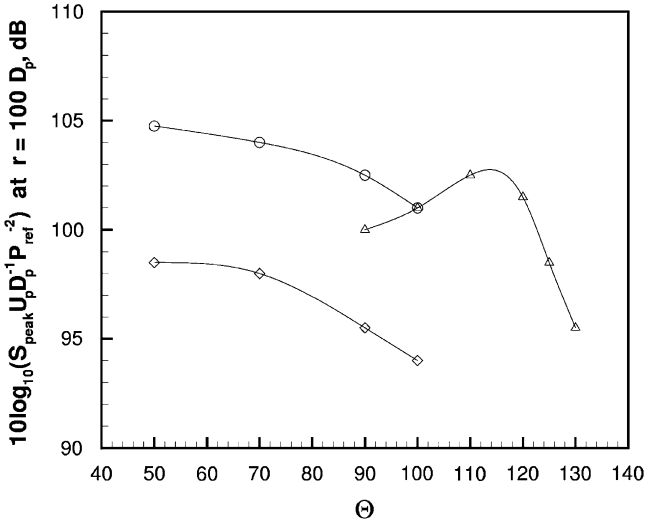

Fig. 10. Variation of maximum sound–pressure-level of broadband shock-cell noise with direction of radiation for a dual stream jet. $M_p = 0.72$, $T_p^{(r)}/T_a = 2.14$, $M_s = 1.36$, $T_s^{(r)}/T_a = 1.0$.

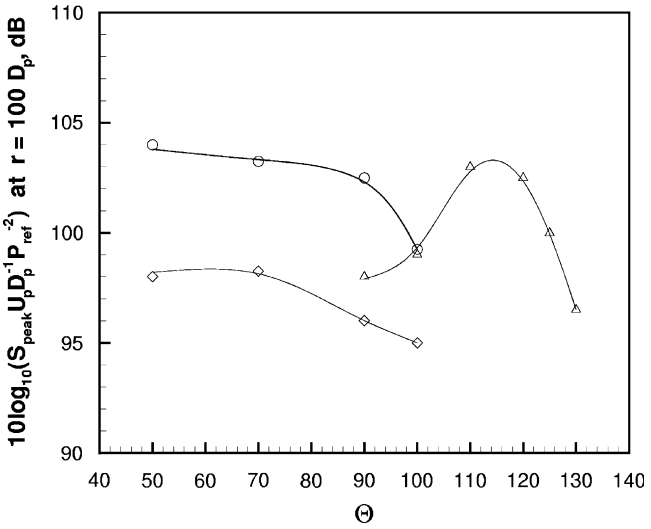

Fig. 11. Variation of maximum sound–pressure-level of broadband shock-cell noise with direction of radiation for a dual stream jet. $M_p = 0.85$, $T_p^{(r)}/T_a = 2.26$, $M_s = 1.36$, $T_s^{(r)}/T_a = 1.0$.

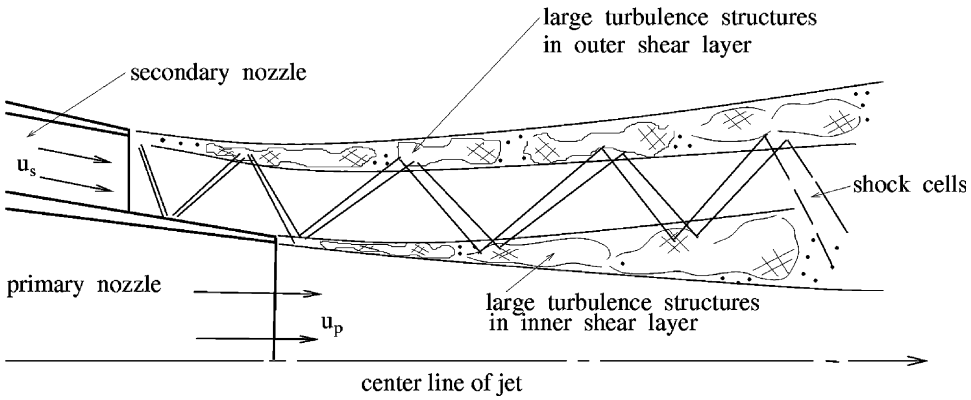

Fig. 12. Schematic diagram of a dual stream jet showing shock cells in the secondary stream and large turbulence structures in the outer and inner shear layers.

For jets with a supersonic secondary stream and a subsonic primary stream, a shock-cell structure will form in the supersonic region of the secondary jet as shown in Fig. 12. The shock cells are initiated primarily at the exit of the secondary nozzle due to pressure mismatch between that of the jet at the nozzle exit and that of the ambient air. The expansion wave from the lip of the secondary nozzle propagates across the jet and is reflected back into the jet stream by the nozzle wall. Subsequent reflection by the outer shear layer results in a shock. The shock/expansion wave system may be viewed as compressible disturbances trapped between the inner and outer shear layer. The static ambient air and the subsonic primary jet do not support shocks and expansion waves. These compressible disturbances are therefore reflected back into the supersonic secondary jet stream. The trapped disturbances bounce from one shear layer to the other forming a quasi-periodic shock-cell structure as illustrated in Fig. 12.

Let $p_s(r, x)$ denote the pressure perturbation of the shock/expansion wave system in the jet plume. A simple mathematical representation of the quasi-periodic component of the shock-cell structure is to expand p_s as a generalized Fourier series; i.e.,

$$p_s = \sum_{n=1}^{\infty} A_n \phi_n(r) \cos(\lambda_n x) = \sum_{n=1}^{\infty} \frac{1}{2} A_n \phi_n(r)(e^{i\lambda_n x} + e^{-i\lambda_n x}) \tag{7}$$

where λ_n is the nth wavenumber (wavelength $= 2\pi/\lambda_n$), $\phi_n(r)$ the normalized radial distribution of the nth Fourier mode of the shock cells, and A_n the mode amplitude. In the case of a single stream jet surrounded by a thin mixing layer (vortex sheet jet), a complete first-order analytical shock-cell solution in the form of Eq. (7) was given by Pack [30] and Tam [32] (see also Tam and Tanna [6]) in terms of Bessel functions. For a dual stream jet with a recessed secondary nozzle, an analytical solution is not available. However, in a recent work by the authors [26], a procedure to compute the shock-cell structure by a CAA method was developed. From the computational solution, it is possible to extract the dominant shock-cell wavenumber λ_n ($n = 1,2,3,\ldots$). Thus, the basic periodicity of the shock-cell system may be computed readily.

It is known since the pioneering work of Crow and Champagne [37] and Brown and Roshko [38] that the dynamics of a turbulent shear layer is controlled by the large turbulence structures. Recent optical observations by Thurow et al. [39] and others gave the size of the large turbulence structures in the axial direction to be of the order of the jet diameter. The correlation length as estimated from the radiated sound field by Tam et al. [40] is slightly more than two diameters. The large turbulence structures are themselves an important source of jet mixing noise (see the experimental evidence provided by Tam et al. [40]). In the schematic diagram of Fig. 12, the presence of large turbulence structures in both the inner and outer shear layer of the jet is included.

For statistical prediction purposes, Tam and Chen [41] proposed to represent the large turbulence structures by a stochastic instability-wave model. Such a stochastic model was later used by Tam and Chen [42] to study the direct noise radiation from the large turbulence structures of supersonic jets. The underlying idea of the model is that the large turbulence structures are basically instability waves of the mixing layer grown to a nonlinear state. Mathematically, the physical variables of the large turbulence structures are formed by a superposition of the instability wave spectrum of the flow. The amplitudes of the instability waves are, however, taken as stochastic random variables. In essence, this approach allows one to represent the large turbulence structures of the jet mixing layer as wave-like entities. Suppose u_c is the convection velocity of the large turbulence structures and Ω is the dominant frequency, then the pressure fluctuation associated with a component of the structures may be represented by a propagation wave (in the axial direction of the jet) of the form

$$p_{ts} = \mathrm{Re}\left[a\, \mathrm{e}^{\mathrm{i}((x/u_c)-t)\Omega}\right] \tag{8}$$

where Re[ ] is the real part of [ ] and x is the direction of jet flow. a is the wave amplitude which may be treated as a stochastic variable.

Tam and Tanna [6] were the first to propose that broadband shock-cell noise is generated by the interaction of the large turbulence structures and the shock cells in the jet plume as the former pass through the latter. The interaction leads to source terms that are products of the terms of Eqs. (7) and (8). On combining the wave representation of Eq. (8) and the second term of Eq. (7), the source term has the appearance of a traveling wave of the form

$$p_{\mathrm{source}} : A\, \mathrm{e}^{\mathrm{i}[((\Omega/u_c)-\lambda_n)x-\Omega t]}. \tag{9}$$

We would like to point out that in Eq. (9) the wavenumber of the source, k_{source}, is given by

$$k_{\mathrm{source}} = \frac{\Omega}{u_c} - \lambda_n. \tag{10}$$

A dual stream jet has two mixing layers in which interaction between the large turbulence structures of the shear layer and the shock cells may occur. This provides the two sources responsible for the generation of the two components of broadband shock-cell noise discussed in the previous section. The acoustic propagation and radiation processes of each noise component are analyzed below using a simple jet model.

4.2. Noise transmission and radiation model

The passage of large turbulence structures through the shock-cell structure of a dual stream jet produces unsteady disturbances. In the outer shear layer, such disturbances can directly give rise to noise radiation.

In the inner shear layer, the disturbances must first be transmitted through the supersonic secondary jet and the outer shear layer before radiating sound to the far field. An exact or nearly exact analysis of the transmission and radiation processes is highly involved and complicated: it is beyond the scope of this work. The objective of the present investigation is to use a simple vortex sheet jet model for the purpose of analyzing the processes of sound transmission and radiation. Admittedly, such a model is rather crude. However, it seems to be able to retain the important components of the problem including a supersonic mean flow and an inner and outer shear layers. On the other hand, the attractiveness of the model lies in its simplicity. Such a simple model allows the possibility of an analytical solution and the establishment of simple analytical formulas relating radiated sound frequency and directivity, which is a crucial feature of broadband shock-cell noise. It will be shown later that this model also provides an explanation for other experimentally observed features of broadband shock-cell noise.

4.2.1. *Broadband shock-cell noise originated from the outer shear layer*

To determine sound radiation from the wave-like source of Eq. (9) due to the passage of large turbulence structures through the shock cells in the outer shear layer, we will use a vortex sheet model as shown in Fig. 13. In this simplified model, the mixing layers are represented by vortex sheets. The diameter of the outer stream is D_j and the diameter of the primary jet is D_p. For the noise source, we will assume a general pressure

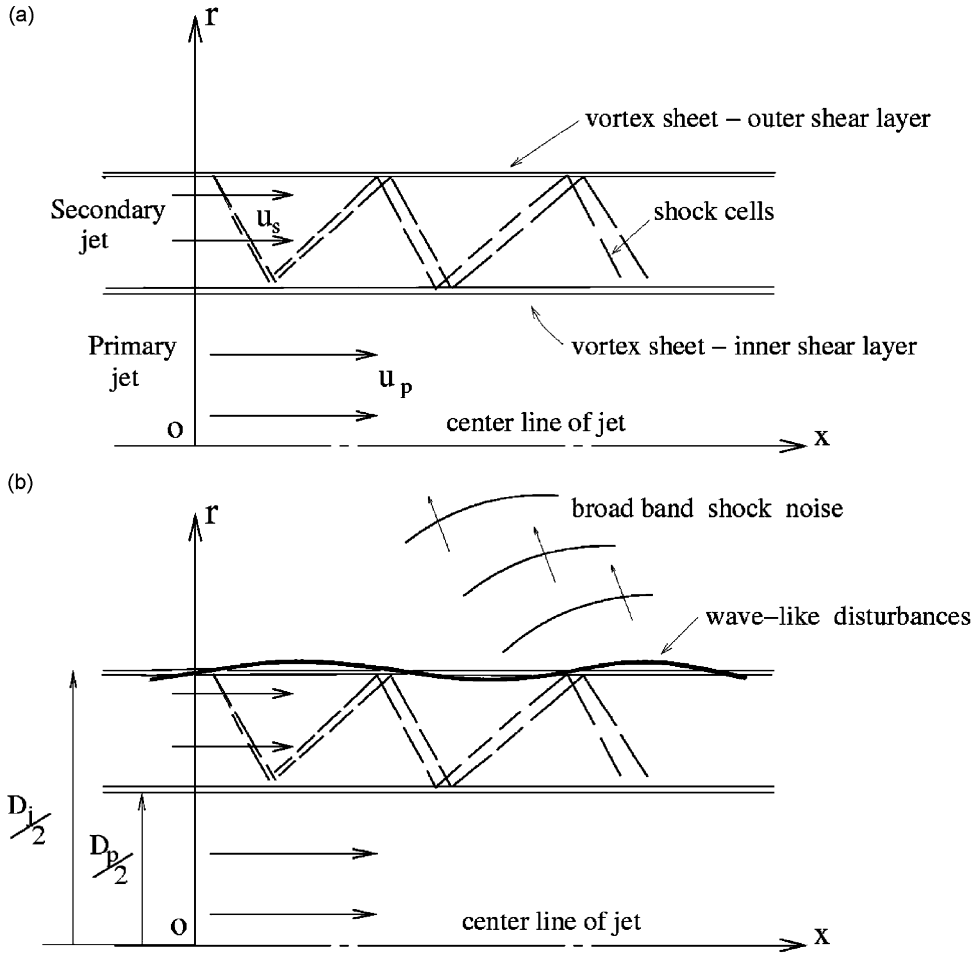

Fig. 13. A vortex sheet dual stream jet model showing: (a) a shock-cell structure in the secondary stream and (b) wave-like disturbances in the outer shear layer and noise radiation.

disturbance of the form

$$p_{\text{source}} = \text{Re}[F(x)\text{e}^{-\text{i}\Omega t}] \tag{11}$$

in the outer shear layer. We will specialize the source to that of a traveling wave in the form of Eq. (9) later.

Outside the jet, acoustic disturbances are governed by the linearized compressible Euler equations. In cylindrical coordinates, they are

$$\frac{\partial \rho}{\partial t} + \rho_0 \left(\frac{\partial v}{\partial r} + \frac{v}{r} + \frac{\partial u}{\partial x} \right) = 0 \tag{12}$$

$$\frac{\partial v}{\partial t} = -\frac{1}{\rho_0} \frac{\partial p}{\partial r} \tag{13}$$

$$\frac{\partial u}{\partial t} = -\frac{1}{\rho_0} \frac{\partial p}{\partial x} \tag{14}$$

$$\frac{\partial p}{\partial t} + \gamma p_0 \left(\frac{\partial v}{\partial r} + \frac{v}{r} + \frac{\partial u}{\partial x} \right) = 0. \tag{15}$$

The boundary conditions for the wave field are

$$r \to \infty, \quad \text{All variables behave like outgoing waves}$$

$$r = \frac{D_j}{2}, \quad p = \text{Re}[F(x)\,\text{e}^{-\text{i}\Omega t}]. \tag{16}$$

It is straightforward to show, by eliminating u and v from Eqs. (12)–(16), that p satisfies the simple wave equation. The solution of the simple wave equation may be found by first letting p to have time dependence of the form

$$p = \text{Re}[\hat{p}(r, x)\text{e}^{-\text{i}\Omega t}]. \tag{17}$$

This allows the time factor $\text{e}^{-\text{i}\Omega t}$ to be separated out. The next step is to apply Fourier transform in x to the reduced simple wave equation and boundary condition (16). The Fourier transforms are

$$\tilde{p}(r, k) = \frac{1}{2\pi} \int_{-\infty}^{\infty} \hat{p}(r, x)\text{e}^{-\text{i}kx}\,\text{d}x \tag{18}$$

$$\tilde{F}(k) = \frac{1}{2\pi} \int_{-\infty}^{\infty} F(x)\text{e}^{-\text{i}kx}\,\text{d}x = \delta(k - k_{\text{source}}). \tag{19}$$

The Fourier transform of the reduced simple wave equation and boundary condition (16) are

$$\frac{\text{d}^2\tilde{p}}{\text{d}r^2} + \frac{1}{r}\frac{\text{d}\tilde{p}}{\text{d}r} + \left(\frac{\Omega^2}{a_\infty^2} - k^2 \right)\tilde{p} = 0 \tag{20}$$

at $r = D_j/2$,

$$\tilde{p} = \tilde{F}(k). \tag{21}$$

The solution of Eq. (20) satisfying boundary condition (21) and the radiation boundary condition at $r \to \infty$ is,

$$\tilde{p}(r, k) = \frac{\tilde{F}(k) H_0^{(1)}\left[\text{i}\left(k^2 - \dfrac{\Omega^2}{a_\infty^2} \right)^{1/2} r \right]}{H_0^{(1)}\left[\text{i}\left(k^2 - \dfrac{\Omega^2}{a_\infty^2} \right)^{1/2} \dfrac{D_j}{2} \right]} \tag{22}$$

where $H_0^{(1)}[\,]$ is the zeroth-order Hankel function of the first kind. In Eq. (22), the branch cuts of the square root function $(k^2-\Omega^2/a_\infty^2)^{1/2}$ in the complex k-plane are shown in Fig. 14. This choice of branch cuts assures that solution (22) is bounded as $r\to\infty$ for any k in the complex k-plane.

The pressure field in the physical domain may be found by inverting the Fourier transform. This leads to

$$p(r,x,t)=\mathrm{Re}\left\{\int_{-\infty}^{\infty}\tilde{F}(k)\left[\frac{H_0^{(1)}\left[\mathrm{i}\left(k^2-\frac{\Omega^2}{a_\infty^2}\right)^{1/2}r\right]}{H_0^{(1)}\left[\mathrm{i}\left(k^2-\frac{\Omega^2}{a_\infty^2}\right)^{1/2}\frac{D_j}{2}\right]}\right]\mathrm{e}^{\mathrm{i}kx-\mathrm{i}\Omega t}\,\mathrm{d}k\right\}. \tag{23}$$

We are interested in the far-field sound. To determine the sound field far from the jet, we will switch the coordinates to a spherical polar coordinate system $(R,\tilde{\theta},\phi)$ with the x-axis as the polar axis. The spherical and cylindrical coordinate systems are related by

$$x=R\cos\tilde{\theta},\quad r=R\sin\tilde{\theta}.$$

For large R, we may use the asymptotic form of the Hankel function in Eq. (23). This gives

$$\underset{R\to\infty}{p}(R,\tilde{\theta},t)$$
$$\sim\mathrm{Re}\left\{\int_{-\infty}^{\infty}\frac{\tilde{F}(k)}{H_0^{(1)}\left[\mathrm{i}\left(k^2-\frac{\Omega^2}{a_\infty^2}\right)^{1/2}\frac{D_j}{2}\right]}\left[\frac{2}{\pi\mathrm{i}R\sin\tilde{\theta}\left(k^2-\frac{\Omega^2}{a_\infty^2}\right)^{1/2}}\right]^{1/2}\mathrm{e}^{\left[-(k^2-(\Omega^2/a_\infty^2))^{1/2}\sin\tilde{\theta}-\mathrm{i}k\cos\tilde{\theta}\right]R-\mathrm{i}\Omega t-\mathrm{i}\pi/4}\,\mathrm{d}k\right\}. \tag{24}$$

The k-integral of Eq. (24) may now be evaluated asymptotically for large R by the method of stationary phase. It is easy to find that the stationary phase value of k, denoted by k_s, is given by

$$k_s=\frac{\Omega}{a_\infty}\cos\tilde{\theta} \tag{25}$$

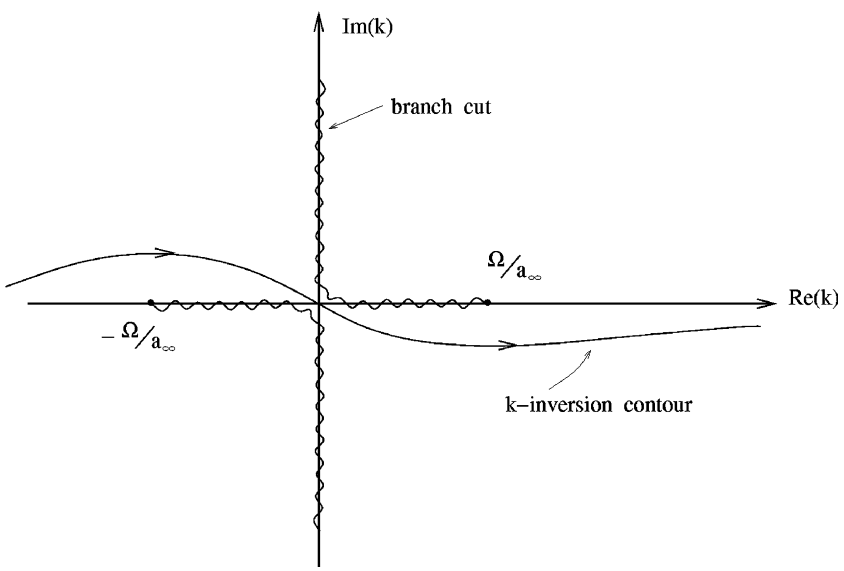

Fig. 14. Branch cuts of the square root function $(k^2-\Omega^2/a_\infty^2)^{1/2}$ in the complex k-plane. Also shown is the Fourier inverse contour.

and the asymptotic integral is

$$\underset{R\to\infty}{p}(R,\tilde{\theta},t)\sim \mathrm{Re}\left\{\frac{2\tilde{F}(k_s)}{R}\frac{1}{H_0^{(1)}\left(\dfrac{\Omega}{a_\infty}\sin\tilde{\theta}\dfrac{D_j}{2}\right)}\mathrm{e}^{\mathrm{i}((R/a_\infty)-t)\Omega-\mathrm{i}\pi/2}\right\}. \tag{26}$$

Eq. (26) is the radiated sound field. The direction of radiation, $\tilde{\theta}$, is related to the source axial wavenumber by Eq. (25).

The source model developed earlier suggests that the dominant axial wavenumber of the source of broadband shock-cell noise generated in the outer shear layer is given by Eq. (10); i.e.,

$$k_{\mathrm{source}}=\frac{\Omega}{u_{\mathrm{outer}}}-\lambda_n. \tag{27}$$

We have used u_{outer} to denote the convection velocity of the large turbulence structures in the outer shear layer. On equating k_s of Eq. (25) and k_{source} of Eq. (27) since $\tilde{F}(k)$ is a delta function, we obtain a relationship between the dominant frequency of radiation (frequency at the peak of the noise spectrum) and the direction of radiation, which may be recast into the following form

$$f_n=\frac{\lambda_n u_{\mathrm{outer}}}{2\pi[1+M_{\mathrm{outer}}\cos\Theta]} \tag{28}$$

where $2\pi f_n=\Omega$, $\Theta=\pi-\tilde{\theta}$ and $M_{\mathrm{outer}}=u_{\mathrm{outer}}/a_\infty$. Eq. (28) is the same as the frequency–directivity relation derived by Tam and Tanna [6] using the Mach angle relation.

4.2.2. Broadband shock-cell noise originated from the inner shear layer

Now, the passage of large turbulence structures in the inner shear layer through the shock-cells will give rise to unsteady disturbances and noise radiation. Within the vortex sheet model (see Fig. 15), we will represent the noise source by the boundary condition

$$r=\frac{D_p}{2},\quad p=\mathrm{Re}[G(x)\mathrm{e}^{-\mathrm{i}\Omega t}] \tag{29}$$

where $G(x)$ is an arbitrary spatial distribution of source strength and Ω the angular frequency. We will specify $G(x)$ to be in the form of a traveling wave as given by Eq. (9) later. We would like to point out again that the

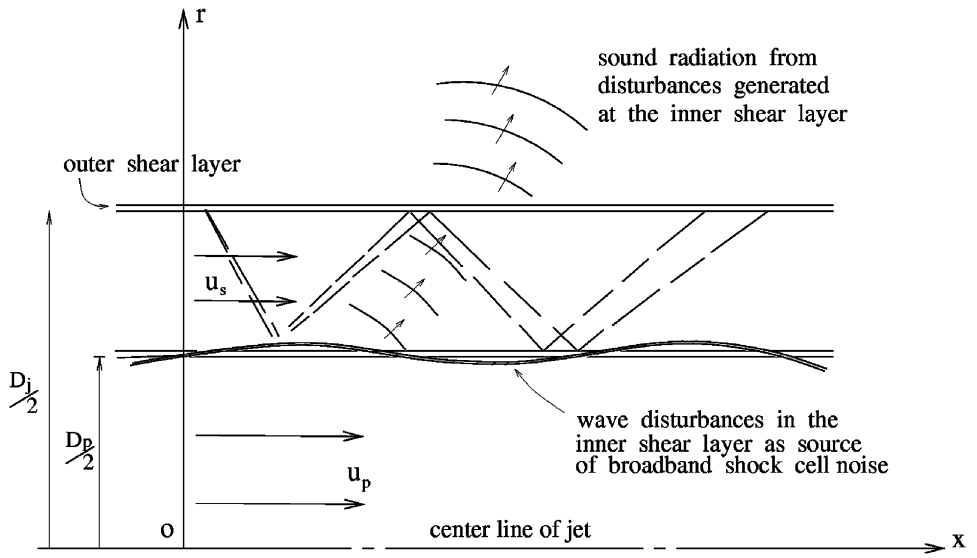

Fig. 15. A vortex sheet dual stream jet model showing wave-like disturbances in the inner shear layer, their transmission through the supersonic secondary jet and noise radiation.

acoustic disturbances generated in the inner shear layer have first to propagate/transmit through the supersonic secondary jet before radiating to the far field as sound. It will be shown that the transmission process imposes special characteristics on the radiated broadband shock-cell noise.

As in the previous section, the governing equations are the linearized compressible Euler equations. To avoid confusion, we will use subscript 1 to denote variables outside the jet ($r \geqslant D_j/2$), subscript 2 to denote variables in the secondary jet. The governing equations in cylindrical coordinates are

$$r \geqslant \frac{D_j}{2}$$

$$\frac{\partial \rho_1}{\partial t} + \rho_0 \left(\frac{\partial v_1}{\partial r} + \frac{v_1}{r} + \frac{\partial u_1}{\partial x} \right) = 0 \tag{30}$$

$$\frac{\partial v_1}{\partial t} = -\frac{1}{\rho_0} \frac{\partial p_1}{\partial r} \tag{31}$$

$$\frac{\partial u_1}{\partial t} = -\frac{1}{\rho_0} \frac{\partial p_1}{\partial x} \tag{32}$$

$$\frac{\partial p_1}{\partial t} + \gamma p_0 \left(\frac{\partial v_1}{\partial r} + \frac{v_1}{r} + \frac{\partial u_1}{\partial x} \right) = 0 \tag{33}$$

where ρ_0, p_0 are the ambient gas density and pressure. γ is the ratio of specific heats.

$$\frac{D_p}{2} \leqslant r \leqslant \frac{D_j}{2}$$

$$\frac{\partial \rho_2}{\partial t} + u_s \frac{\partial \rho_2}{\partial x} + \rho_s \left(\frac{\partial v_2}{\partial r} + \frac{v_2}{r} + \frac{\partial u_2}{\partial x} \right) = 0 \tag{34}$$

$$\frac{\partial v_2}{\partial t} + u_s \frac{\partial v_2}{\partial x} = -\frac{1}{\rho_s} \frac{\partial p_2}{\partial r} \tag{35}$$

$$\frac{\partial u_2}{\partial t} + u_s \frac{\partial u_2}{\partial x} = -\frac{1}{\rho_s} \frac{\partial p_2}{\partial x} \tag{36}$$

$$\frac{\partial p_2}{\partial t} + u_s \frac{\partial p_2}{\partial x} + \gamma p_s \left(\frac{\partial v_2}{\partial r} + \frac{v_2}{r} + \frac{\partial u_2}{\partial x} \right) = 0 \tag{37}$$

where ρ_s, p_s, and u_s are the density, pressure, and mean velocity of the secondary jet. The boundary conditions are

$$\text{at } r = \frac{D_p}{2}, \quad p_2 = \mathrm{Re}[G(x) e^{-\mathrm{i}\Omega t}]. \tag{38}$$

At $r = D_j/2$, we impose the vortex sheet boundary conditions of continuity of pressure and particle displacement. Let $r = \zeta\ (x, t)$ be the position of the vortex sheet, then the dynamic and kinematic boundary conditions are

$$p_1 = p_2 \tag{39}$$

$$\frac{\partial \zeta}{\partial t} = v_1 \tag{40}$$

$$\frac{\partial \zeta}{\partial t} + u_s \frac{\partial \zeta}{\partial x} = v_2. \tag{41}$$

To find a solution of the above problem, we may first separate out time dependence by looking for solutions of the form

$$\begin{bmatrix} p_1 \\ v_1 \\ u_1 \\ p_2 \\ v_2 \\ u_2 \\ \zeta \end{bmatrix} = \mathrm{Re}\left\{ \begin{bmatrix} \hat{p}_1(r,x) \\ \hat{v}_1(r,x) \\ \hat{u}_1(r,x) \\ \hat{p}_2(r,x) \\ \hat{v}_2(r,x) \\ \hat{u}_2(r,x) \\ \hat{\zeta}(x) \end{bmatrix} \mathrm{e}^{-\mathrm{i}\Omega t} \right\}. \tag{42}$$

By substitution of Eq. (42) into Eqs. (31)–(41) and on applying Fourier transform in x, after factoring out time dependence $\mathrm{e}^{-\mathrm{i}\Omega t}$ and on eliminating other variables, the problem becomes ($a\sim$over a variable will be used to denote a Fourier transformed variable).

$$\frac{D_j}{2} \leqslant r, \quad \frac{\mathrm{d}^2\tilde{p}_1}{\mathrm{d}r^2} + \frac{1}{r}\frac{\mathrm{d}\tilde{p}_1}{\mathrm{d}r} + \left(\frac{\Omega^2}{a_\infty^2} - k^2\right)\tilde{p}_1 = 0 \tag{43}$$

$$\tilde{v}_1 = -\frac{\mathrm{i}}{\rho_0\Omega}\frac{\mathrm{d}\tilde{p}_1}{\mathrm{d}r} \tag{44}$$

where $a_\infty = (\gamma p_0/\rho_0)^{1/2}$ is the ambient sound speed.

$$\frac{D_p}{2} \leqslant r \leqslant \frac{D_j}{2}, \quad \frac{\mathrm{d}^2\tilde{p}_2}{\mathrm{d}r^2} + \frac{1}{r}\frac{\mathrm{d}\tilde{p}_2}{\mathrm{d}r} + \left[\frac{(u_s k - \Omega)^2}{a_s^2} - k^2\right]\tilde{p}_2 = 0 \tag{45}$$

$$\tilde{v}_2 = \frac{-\mathrm{i}}{\rho_s(\Omega - u_s k)}\frac{\mathrm{d}\tilde{p}_2}{\mathrm{d}r} \tag{46}$$

where k is the Fourier transform variable and a_s is the speed of sound in the secondary jet. The boundary conditions are

$$\text{at} \quad r = \frac{D_p}{2}, \quad \tilde{p}_2 = \tilde{G}(k) = \frac{1}{2\pi}\int_{-\infty}^{\infty} G(x)\mathrm{e}^{\mathrm{i}kx}\,\mathrm{d}x = \delta(k - k_{\text{source}}) \tag{47}$$

$$\text{at } r = \frac{D_j}{2}, \quad \tilde{p}_1 = \tilde{p}_2 \tag{48}$$

$$\frac{\tilde{v}_1}{\Omega} = \frac{\tilde{v}_2}{\Omega - k u_s}. \tag{49}$$

The solution of Eqs. (43) and (44) that satisfies radiation boundary conditions at $r \to \infty$ is

$$\tilde{p}_1 = A(k)H_0^{(1)}\left[\mathrm{i}\left(k^2 - \frac{\Omega^2}{a_\infty^2}\right)^{1/2} r\right] \tag{50}$$

$$\tilde{v}_1 = \frac{A(k)\left(k^2 - \dfrac{\Omega^2}{a_\infty^2}\right)^{1/2}}{\rho_0\Omega} H_0^{(1)'}\left[\mathrm{i}\left(k^2 - \frac{\Omega^2}{a_\infty^2}\right)^{1/2} r\right] \tag{51}$$

where $'$ denotes the derivative. The branch cuts for $(k^2 - \Omega^2/a_\infty^2)^{1/2}$ in the k-plane are as shown in Fig. 14.

The solution of Eqs. (45)–(49) is

$$\tilde{p}_2 = B(k)H_0^{(1)}[(M_s^2 - 1)^{1/2}(k - k_-)^{1/2}(k - k_+)^{1/2} r] + C(k)H_0^{(2)}[(M_s^2 - 1)^{1/2}(k - k_-)^{1/2}(k - k_+)^{1/2} r] \tag{52}$$

where

$$k_- = \frac{\Omega/a_s}{M_s - 1}, \quad k_+ = \frac{\Omega/a_s}{M_s + 1}.$$

In Eq. (52), M_s is the Mach number of the secondary jet. $H_0^{(1)}[\ ]$ and $H_0^{(2)}[\ ]$ are the zeroth-order Hankel function of the first and second kind.

$$\tilde{v}_2 = \frac{-\mathrm{i}(M_s^2-1)^{1/2}(k-k_-)^{1/2}(k-k_+)^{1/2}}{\rho_s(\Omega - ku_s)}\{B(k)H_0^{(1)'}[(M_s^2-1)^{1/2}(k-k_-)^{1/2}(k-k_+)^{1/2}r] + C(k)H_0^{(2)'}[(M_s^2-1)^{1/2}(k-k_-)^{1/2}(k-k_+)^{1/2}r]\}. \tag{53}$$

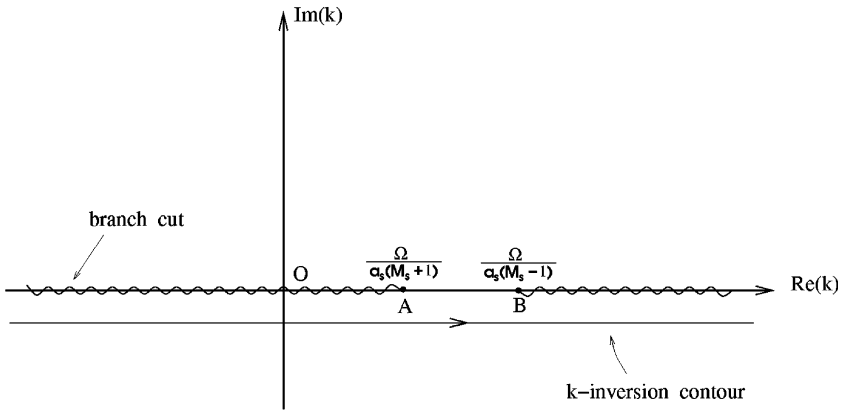

Fig. 16. Branch cuts of the square root function $(k-k_-)^{1/2}(k-k_+)^{1/2}$ where $k_+ = \Omega/a_s(M_s+1)$, and $k_- = \Omega/a_s(M_s-1)$ in the complex k-plane. Also shown is the Fourier inverse contour.

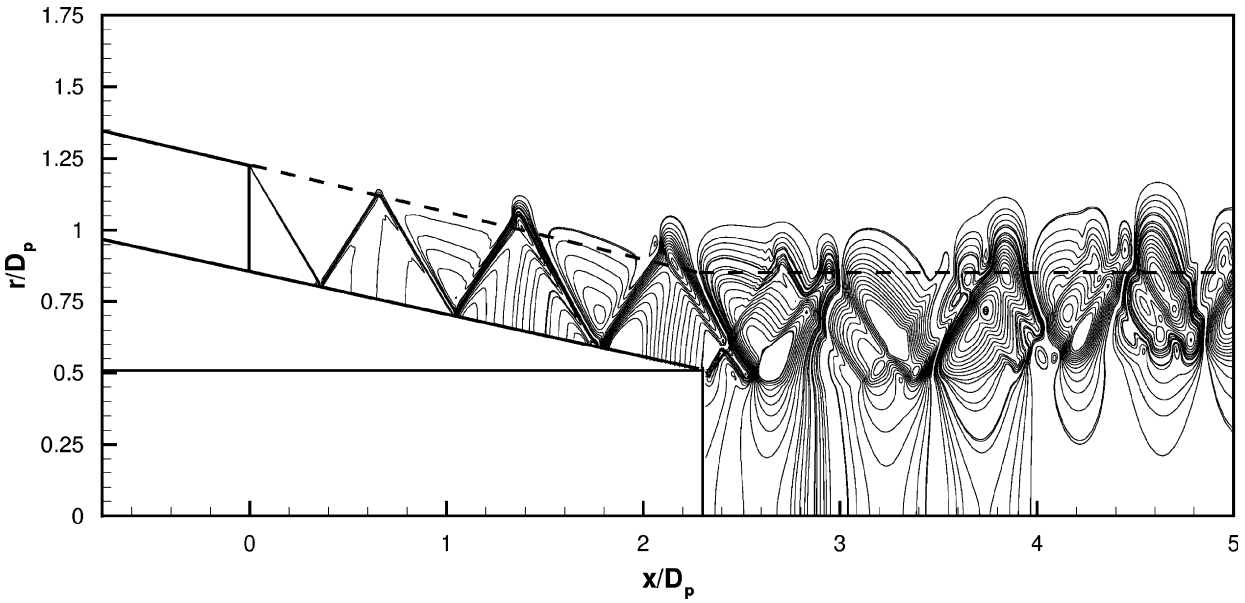

Fig. 17. Pressure contours of the shock cells of a dual stream jet at $M_p = 0.72$, $T_p^{(r)}/T_a = 2.14$, $M_s = 1.36$, $T_s^{(r)}/T_a = 1.0$. The dotted line is the lip line of the secondary jet.

The branch cuts for the square root function $(k-k_-)^{1/2}(k_--k_+)^{1/2}$ are as shown in Fig. 16. Also shown in this figure is the k-inversion (Fourier inverse transform) contour. The boundary conditions are given by Eqs. (47)–(49). These three boundary conditions are to determine the three unknowns $A(k)$, $B(k)$, and $C(k)$.

Now, the first term on the right side of the solution (52) represents a wave propagating in the direction of r for k lying on the inversion k-contour to the left of branch point 'A' at $k=(\Omega/a_s)/(M_s+1)$. At the same time, the second term represents a wave propagating in the opposite direction. With this understanding, we will require the outgoing solution Eq. (52) to match the source pressure of Eq. (47). The second solution of Eq. (52) is the reflected wave created when the outgoing wave reaches the outer shear layer. Thus on enforcing boundary conditions (47)–(49), we find, after some algebra

$$A(k)=\frac{-4\mathrm{i}\tilde{G}(k)}{\pi(M_s^2-1)^{1/2}(k-k_-)^{1/2}(k-k_+)^{1/2}\dfrac{D_j}{2}H_0^{(1)}\left[(M_s^2-1)^{1/2}(k-k_-)^{1/2}(k-k_+)^{1/2}\dfrac{D_p}{2}\right]}\frac{1}{\Phi(k)}\frac{1}{} \tag{54}$$

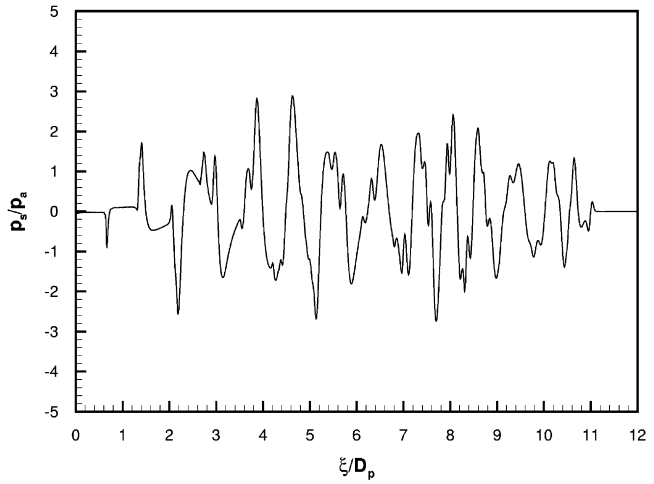

Fig. 18. Pressure distribution along the lip line of the jet of Fig. 17.

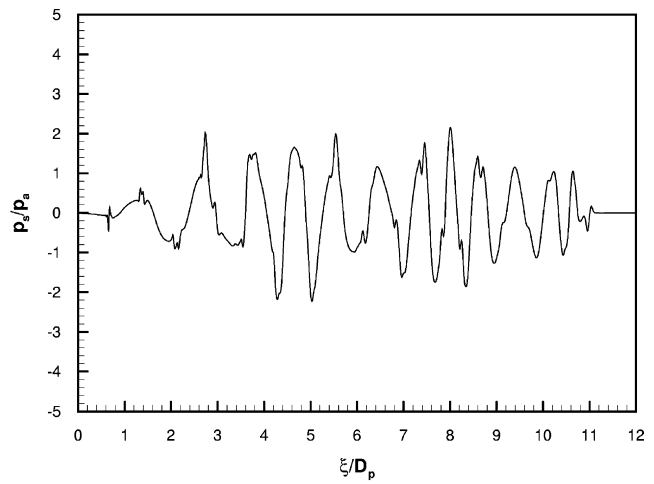

Fig. 19. Pressure distribution of the first Fourier mode along the lip line of the jet of Fig. 17.

$$\Phi(k) = H_0^{(1)}\left[\mathrm{i}\left(k^2 - \frac{\Omega^2}{a_\infty^2}\right)^{1/2}\frac{D_j}{2}\right]H_0^{(2)'}\left[(M_s^2-1)^{1/2}(k-k_-)^{1/2}(k-k_+)^{1/2}\frac{D_j}{2}\right]$$
$$-\frac{\mathrm{i}\rho_s(\Omega-u_s k)}{\rho_0\Omega}\frac{\left(k^2-\dfrac{\Omega^2}{a_\infty^2}\right)^{1/2}}{(M_s^2-1)^{1/2}(k-k_-)^{1/2}(k-k_+)^{1/2}}H_0^{(1)'}\left[\mathrm{i}\left(k^2-\frac{\Omega^2}{a_\infty^2}\right)^{1/2}\frac{D_j}{2}\right]$$
$$\times H_0^{(2)}\left[(M_s^2-1)^{1/2}(k-k_-)^{1/2}(k-k_+)^{1/2}\frac{D_j}{2}\right]. \tag{55}$$

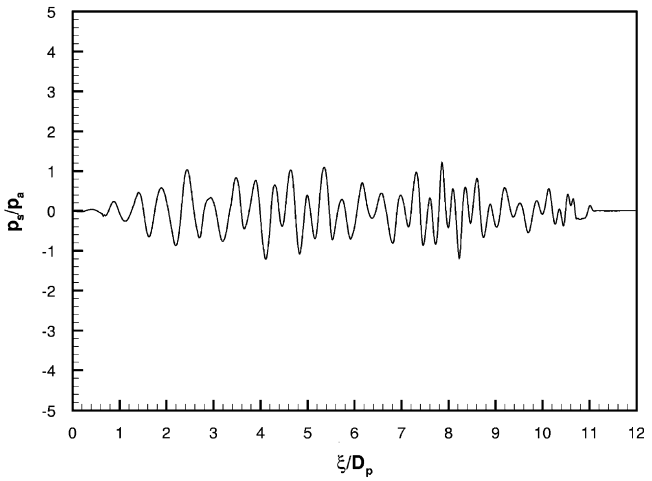

Fig. 20. Pressure distribution of the second Fourier mode along the lip line of the jet of Fig. 17.

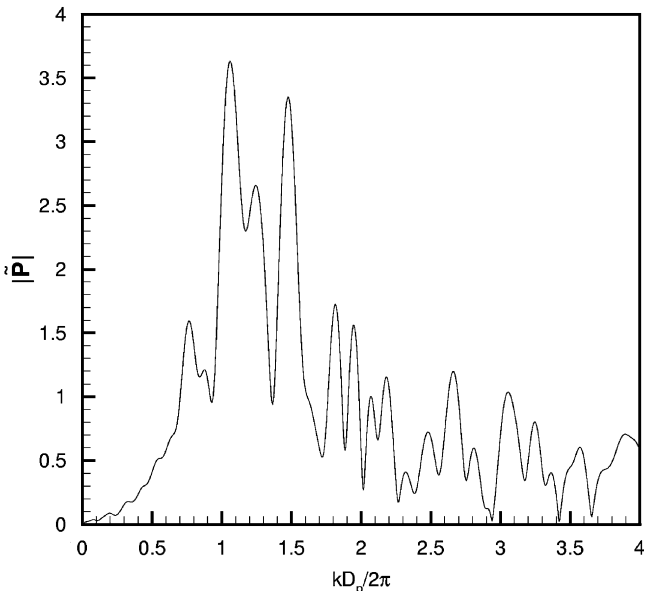

Fig. 21. Absolute value (wavenumber spectrum) of the Fourier transform of the pressure distribution of Fig. 18.

Outside the jet, for $R\to\infty$, the acoustic field is given by the inverse Fourier transform of Eq. (50); i.e., (in spherical polar coordinates)

$$\underset{R\to\infty}{p_1}(R,\tilde{\theta},t)\sim \mathrm{Re}\left\{\int_{-\infty}^{\infty}\left[\frac{2}{\pi \mathrm{i}\, R\sin\tilde{\theta}\left(k^2-\dfrac{\Omega^2}{a_\infty^2}\right)^{1/2}}\right]^{1/2} A(k)\mathrm{e}^{[-(k^2-\frac{\Omega^2}{a_\infty^2})^{1/2}\sin\tilde{\theta}+\mathrm{i}k\cos\tilde{\theta}]R-\mathrm{i}\Omega t}\,\mathrm{d}k\right\} \tag{56}$$

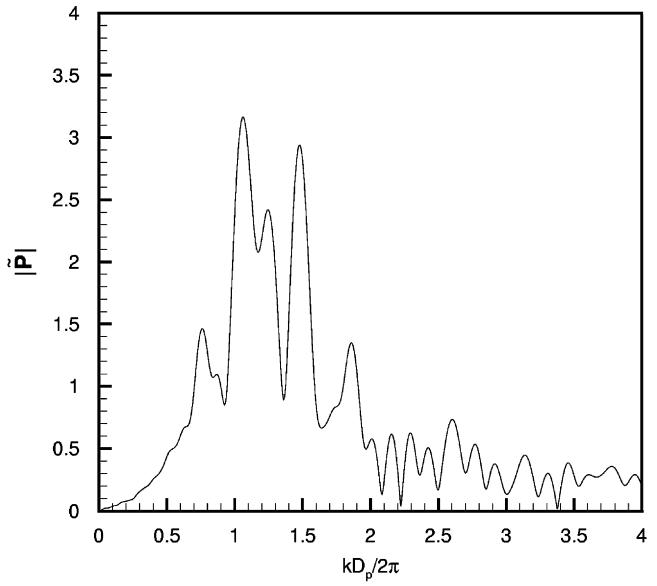

Fig. 22. Absolute value (wavenumber spectrum) of the Fourier transform of the pressure distribution of Fig. 19.

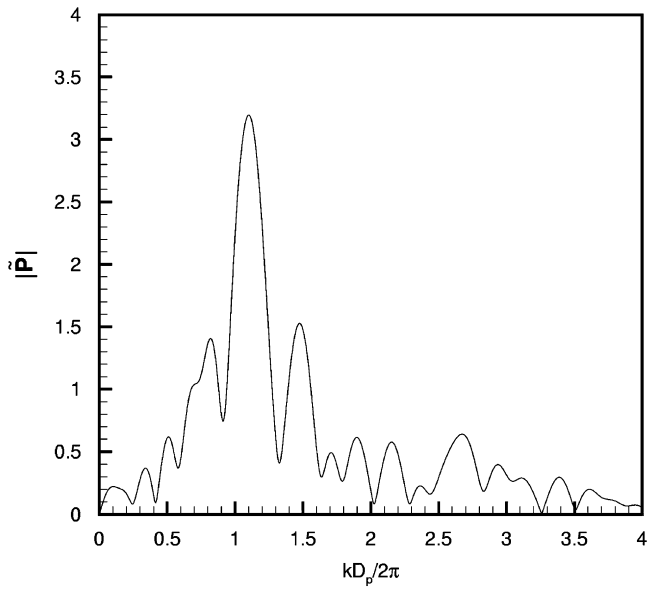

Fig. 23. Absolute value (wavenumber spectrum) of the Fourier transform of the pressure distribution of Fig. 19. The sample interval is $0\leqslant x/D_p\leqslant 7.9$.

where the asymptotic form of the Hankel function has been used. For large R, the integral above may be evaluated by the method of stationary phase as before. The stationary phase point, k_s, is given by Eq. (25); i.e.,

$$k_s = \frac{\Omega}{a_\infty}\cos\tilde{\theta} \tag{57}$$

where k_s is the axial wavenumber of the source. The sound field is

$$\underset{R\to\infty}{p_1}(R,\tilde{\theta},\phi)\sim \mathrm{Re}\left\{\frac{2A(k_s)}{R}e^{\mathrm{i}(R/a_\infty - t)\Omega - \mathrm{i}\pi/4}\right\} \tag{58}$$

provided the stationary phase point k_s lies to the left of point A in Fig. 16.

Now the source wavenumber, k_{source}, is given by Eq. (10); i.e.,

$$k_{\mathrm{source}} = \frac{\Omega}{u_{\mathrm{inner}}} - \lambda_n \tag{59}$$

where u_{inner} is the convection velocity of the large turbulence structures in the inner shear layer. Therefore, by equating k_s of Eq. (57) to k_{source} of Eq. (59), because $\tilde{G}(k)$ is a delta function, it is found

$$f_n = \frac{\lambda_n u_{\mathrm{inner}}}{2\pi[1 + M_{\mathrm{inner}}\cos\Theta]} \tag{60}$$

where f_n is the peak noise frequency corresponding to the nth shock-cell mode and $M_{\mathrm{inner}} = u_{\mathrm{inner}}/a_s$ the convective Mach number of the large turbulence structure of the inner shear layer. Eq. (60) is formally the same as Eq. (28) except that u_{outer} is replaced by u_{inner}. In general $u_{\mathrm{inner}} \neq u_{\mathrm{outer}}$ so that the frequency–directivity relation for broadband shock-cell noise generated in the inner shear layer is different from that generated in the outer shear layer. Because the disturbances from the inner layer have to propagate through the supersonic secondary jet, disturbances with negative phase velocity; i.e., $k_s < 0$ are severely restricted. Thus by Eq. (57), there is little radiation in directions for which

$$\cos\tilde{\theta} < 0; \quad \text{i.e.,} \quad \tilde{\theta} > \pi/2 \quad \text{or} \quad \Theta < \pi/2. \tag{61}$$

Furthermore, for k_s greater than the branch point at 'A', i.e. $k_+ = [(\Omega/a_s)/(M_s+1)]$, the square root function $(k-k_-)^{1/2}(k-k_+)^{1/2}$ becomes purely imaginary. This makes the outgoing wave solution $H_0^{(1)}[(M_s^2-1)^{1/2}(k-k_-)^{1/2}(k-k_+)^{1/2}r]$ to decay exponentially with r. In other words, $A(k_s)$ of Eq. (58) will become smaller

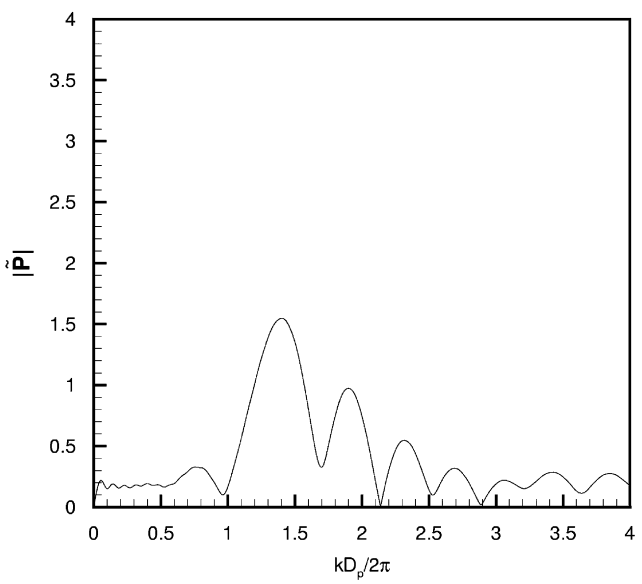

Fig. 24. Absolute value (wavenumber spectrum) of the Fourier transform of the pressure distribution of Fig. 19. The sample interval is $7.9 \leqslant x/D_p \leqslant 21$.

and smaller as k_s becomes larger and larger than k_+. Since k_s is related to the direction of radiation $\tilde{\theta}$ by Eq. (57), this means that there is a roll-off of broadband shock-cell noise for $\tilde{\theta}<\tilde{\theta}_{\text{roll-off}}$ where $\tilde{\theta}_{\text{roll-off}}$ is given by

$$k_{\text{roll-off}} = \frac{\Omega}{a_\infty}\cos\,\tilde{\theta}_{\text{roll-off}} = \frac{\Omega}{a_s}\frac{1}{1+M_s}.$$

Thus

$$\tilde{\theta}_{\text{roll-off}} = \pi - \Theta_{\text{roll-off}} = \cos^{-1}\left[\frac{a_\infty}{a_s(1+M_s)}\right] \tag{62}$$

where $\Theta_{\text{roll-off}}$ is the inlet roll-off angle.

There is a physical explanation of the roll-off phenomenon. The wavenumber of the branch point is $k_s = k_+ = (\Omega/a_s)/(M_s+1)$. For a wave with wavenumber k_s, the phase speed relative to the nozzle fixed coordinate system is Ω/k_s. Therefore, relative to the secondary jet with a velocity u_s the phase speed is $[(\Omega/k_s)-u_s]$. This speed will be subsonic if

$$\frac{\Omega}{k_s} - u_s < a_s \quad \text{or} \quad k_s > \frac{\Omega/a_s}{(M_s+1)}. \tag{63}$$

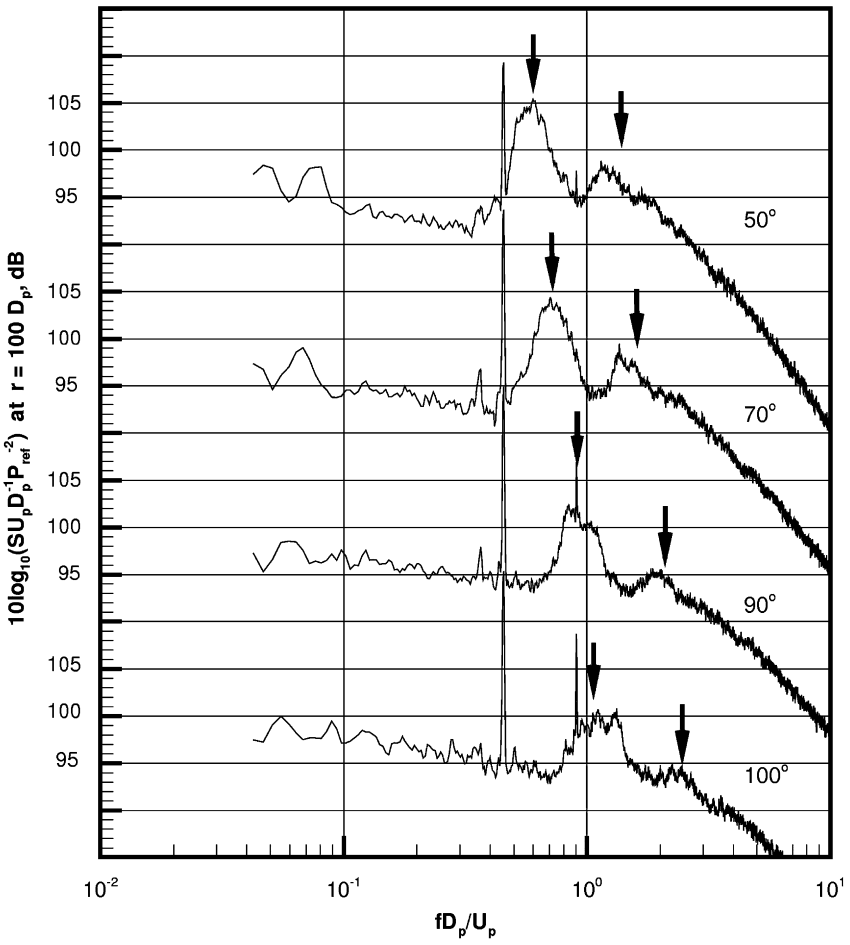

Fig. 25. Comparison of computed and measured peak frequencies of broadband shock-cell noise from a dual stream jet at $M_p = 0.72$, $T_p^{(r)}/T_a = 2.14$, $M_s = 1.36$, $T_s^{(r)}/T_a = 1.0$. Computed peak frequencies are indicated by arrows.

Hence, when the stationary phase point or source point is to the right of the branch point $(\Omega/a_s)[M_s+1]^{-1}$, the wave-like source disturbance is a subsonic wave as far as the secondary jet is concerned. In Appendix A, it is shown that disturbances associated with a subsonic wave decrease exponentially in the direction normal to the jet flow direction. In other words, not all the disturbances generated in the inner shear layer would be transmitted through the secondary jet. This is the reason for the roll-off in broadband shock-cell noise at large inlet angle.

5. Comparison with experimental measurements

5.1. Shock-cell wavenumber analysis

In a recent work, the present authors [26] developed a CAA method to compute the shock-cell structure of dual stream jets. Fig. 17 shows the computed pressure contour pattern of the shock-cell structure of a dual stream jet issued from a nozzle with a cross-sectional configuration as in Fig. 5. The jet operating conditions are $M_p=0.72$, $T_p^{(r)}/T_a=2.14$, $M_s=1.36$, $T_s^{(r)}/T_a=1.0$. It is clear that because the secondary jet nozzle is recessed, the shock-cell structure downstream of the primary nozzle exit is fairly complex. That the shock-cell structure has, indeed, a very complex pattern can also be seen from a measurement of the static pressure distribution (above the ambient pressure) along the lip line (dotted line in Fig. 17) of the jet. This is shown in Fig. 18. In this figure, there are a lot of irregularities both in the amplitudes of the shocks and expansion fans

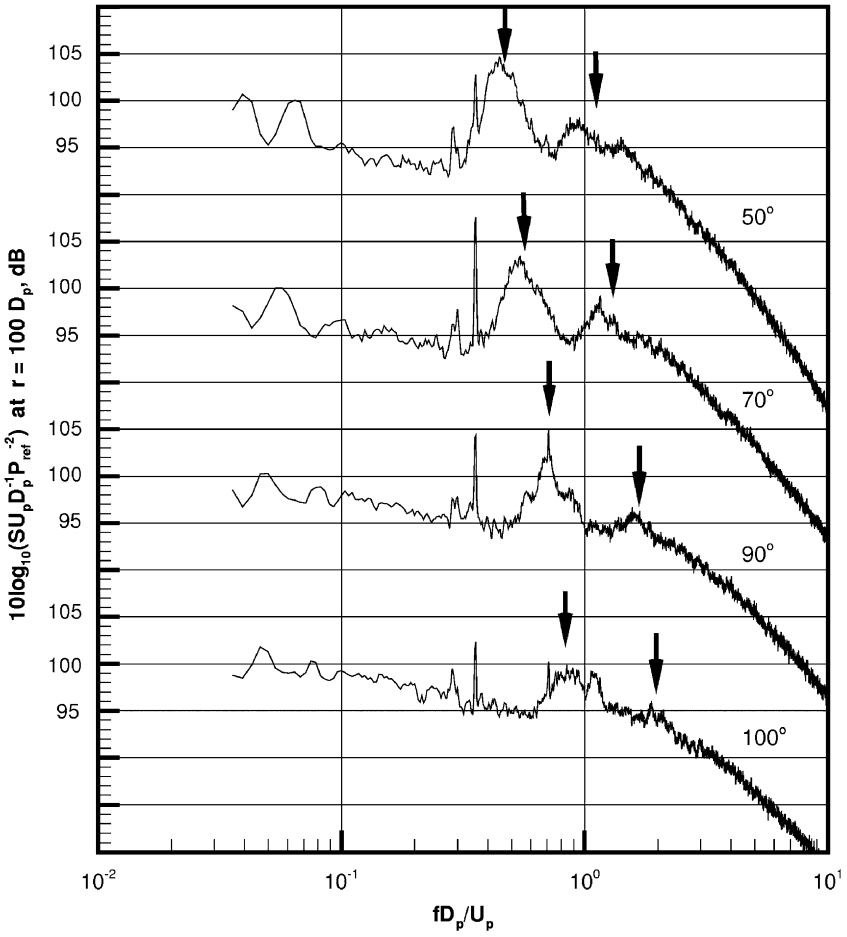

Fig. 26. Comparison of computed and measured peak frequencies of broadband shock-cell noise from a dual stream jet at $M_p=0.85$, $T_p^{(r)}/T_a=2.26$, $M_s=1.36$, $T_s^{(r)}/T_a=1.0$. Computed peak frequencies are indicated by arrows.

as well as in the spacing of the shock cells. Since it is the interaction of the periodic components of the shock-cell structure and the large turbulence structures in the shear layer of the jet that is responsible for the generation of broadband shock-cell noise, it is important to perform a wavenumber analysis to determine the periodic component. In the recent work of Tam et al. [26], the shock-cell structure was decomposed into Fourier modes as a first step in extracting the periodic components of the shock cells. Figs. 19 and 20 show the pressure distributions along the lip line of the jet for the first and second Fourier mode. By comparison with Fig. 18, it appears that Fourier mode decomposition does remove some of the irregularities in the pressure distribution.

To determine the wavenumber spectrum of the shock cells, a Fourier transform of the pressure distribution of Fig. 18 is performed. The absolute value of the Fourier transform, $|\tilde{p}|$, as a function of $(kD_p)/(2\pi)$, where k is the wavenumber or Fourier transform variable, is shown in Fig. 21. As expected, the spectrum contains many peaks. For this reason, it is not very helpful. Fig. 22 shows a similar wavenumber spectrum for the first Fourier mode shown in Fig. 19. This spectrum is, however, quite similar to Fig. 21 except that some of the minor peaks are absent. At this point, it is important to point out that the purpose of the wavenumber analysis is to find the periodic components of the shock-cell structure that are relevant to broadband shock-cell noise generation. For this objective, the wavenumbers that are of interest to us are those in the noise-producing region of the jet. The shock-cell noise producing region is obviously not determined by the length of the shock-cell structure. The large turbulence structures of the jet flow are most energetic only in the core region of the jet. This is shorter than the supersonic core or the entire length of the shock-cell structure. In other words, some of the

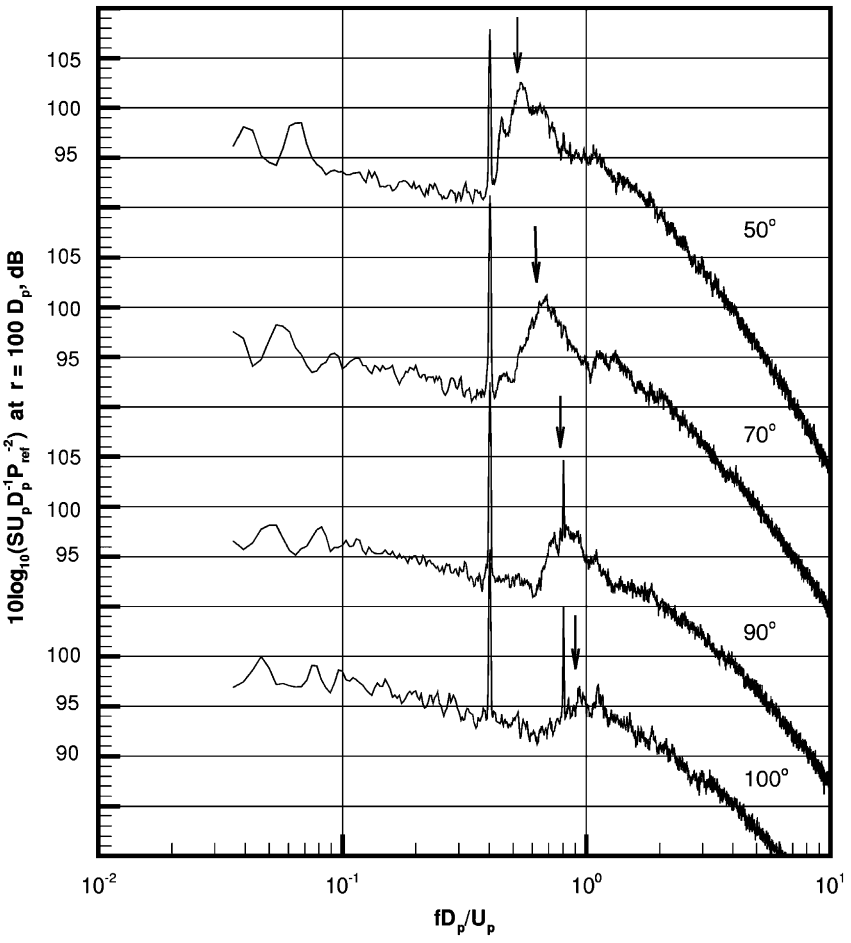

Fig. 27. Comparison of computed and measured peak frequencies of broadband shock-cell noise from a dual stream jet at $M_p = 0.85$, $T_p^{(r)}/T_a = 2.26$, $M_s = 1.28$, $T_s^{(r)}/T_a = 1.0$. Computed peak frequencies are indicated by arrows.

spectral peaks of Fig. 22 that comes from the downstream part of the shock-cell structure may not be relevant to us. Fig. 23 shows the Fourier spectrum of the pressure distribution, along the lip line, of the first Fourier mode with a sample interval $0 \leqslant x/D_p \leqslant 7.9$. This length corresponds approximately to the first 7 shock cells. Fig. 24 shows the Fourier spectrum for the sample interval of $7.9 \leqslant x/D_p \leqslant 21$ (end of shock-cell structure). By comparing Figs. 22–24, it becomes clear that the spectral peak at $kD_p/2\pi = 1.5$ in Fig. 22 comes from the downstream shock-cells. They are not in the shock-cell noise-producing region of the jet. Thus the first peak wavenumber of the shock-cells that is important to shock-cell noise generation is the main peak in Fig. 23. The peak value is at $kD_p/2\pi = 1.125$. By processing the shock-cell data in a similar way, the second peak value of the shock-cell wavenumber spectrum is found to be at $kD_p/2\pi = 2.6$. In the next subsection, the principal shock-cell wavenumbers of dual stream jets, determined by the procedure just described, are used to calculate the peak frequencies of the noise spectrum for comparison with experimental measurements.

5.2. Comparison of peak frequency–directivity relations with experiment

In Section 4, equations linking peak frequencies of broadband shock-cell noise and direction of radiation are derived. Formula (28) is such a relation for noise generated in the outer shear layer and formula (60) is for noise generated in the inner shear layer. Here these formulas will be tested by comparing their predictions with experiments.

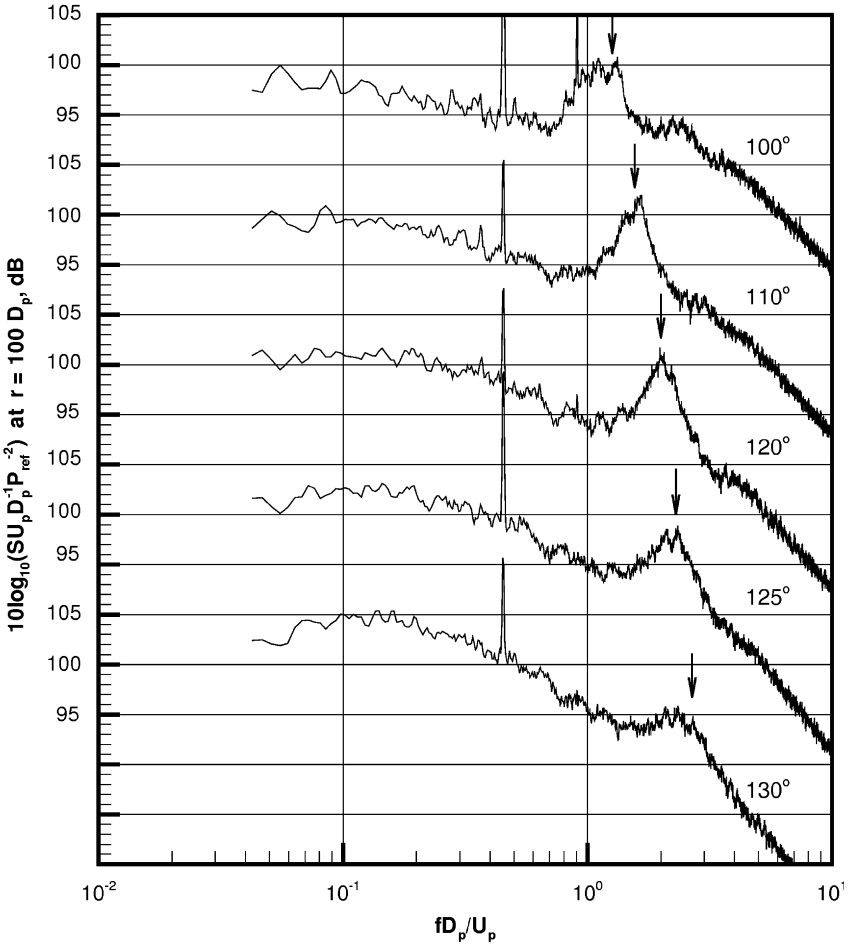

Fig. 28. Comparison of computed and measured peak frequencies of broadband shock-cell noise from a dual stream jet at $M_p = 0.72$, $T_p^{(r)}/T_a = 2.14$, $M_s = 1.36$, $T_s^{(r)}/T_a = 1.0$. Computed peak frequencies are indicated by arrows.

For single stream jets operating at low supersonic Mach number and a total temperature equal to ambient temperature, it is known that the large turbulence structures of the jet flow has a convection velocity nearly equal to 0.7 of the fully expanded jet velocity [13,15]. For dual stream jets with a cold supersonic secondary stream, this empirical convection velocity formula should apply to the large turbulence structures in the outer shear layer. Now with $u_c = 0.7u_s$ and shock-cell wavenumber λ_n ($n = 1,2,3,\ldots$) computed as described above, the peak frequencies of broadband shock-cell noise from the outer shear layer may easily be calculated by Eq. (28). Fig. 25 shows a comparison between the peak noise frequencies computed according to formula (28) and experimental measurements. In this case, the jet operating conditions are: $M_p = 0.72$, $T_p^{(r)}/T_a = 2.14$, $M_s = 1.36$, $T_s^{(r)}/T_a = 1.0$. The black arrows in this figure indicate the computed peak frequencies. Figs. 26 and 27 show similar comparisons at two other jet operating conditions. For Fig. 26, the jet Mach numbers and temperature ratios are: $M_p = 0.85$, $T_p^{(r)}/T_a = 2.26$, $M_s = 1.36$, $T_s^{(r)}/T_a = 1.0$. The jet operating conditions for Fig. 27 are: $M_p = 0.85$, $T_p^{(r)}/T_a = 2.26$, $M_s = 1.28$, $T_s^{(r)}/T_a = 1.0$. As can be seen, the predictions of formula (28) are in good agreement with the experimental measurements.

Broadband shock-cell noise from the inner shear layer is radiated mainly in the downstream direction. The peak frequency for a given direction of radiation is given by formula (60). The inner shear layer separates a hot primary jet and a cold secondary jet. Because of the presence of a strong density gradient, there is no known simple way to compute the convection velocity of the large turbulence structures of the flow. For this reason, formula (60) cannot be used directly to compute the peak frequencies. In this work, an empirical value of u_{inner} is chosen for best fit to the data. The results for the same jet as in Figs. 25–27 are shown in Figs. 28–30.

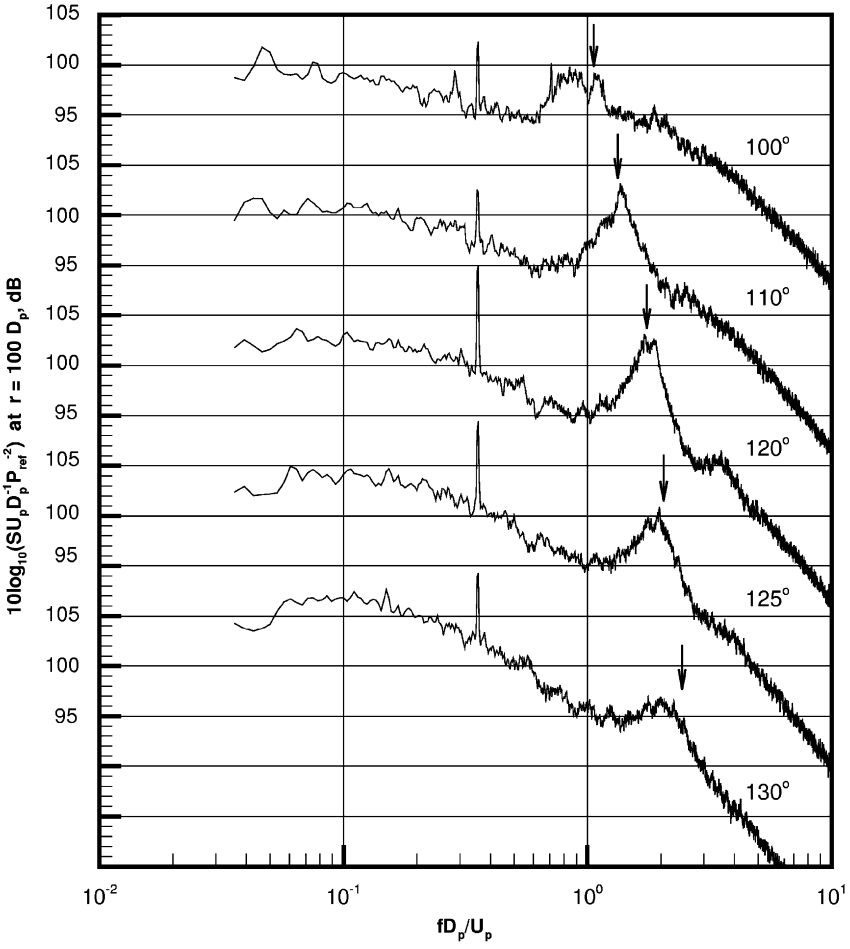

Fig. 29. Comparison of computed and measured peak frequencies of broadband shock-cell noise from a dual stream jet at $M_p = 0.85$, $T_p^{(r)}/T_a = 2.26$, $M_s = 1.36$, $T_s^{(r)}/T_a = 1.0$. Computed peak frequencies are indicated by arrows.

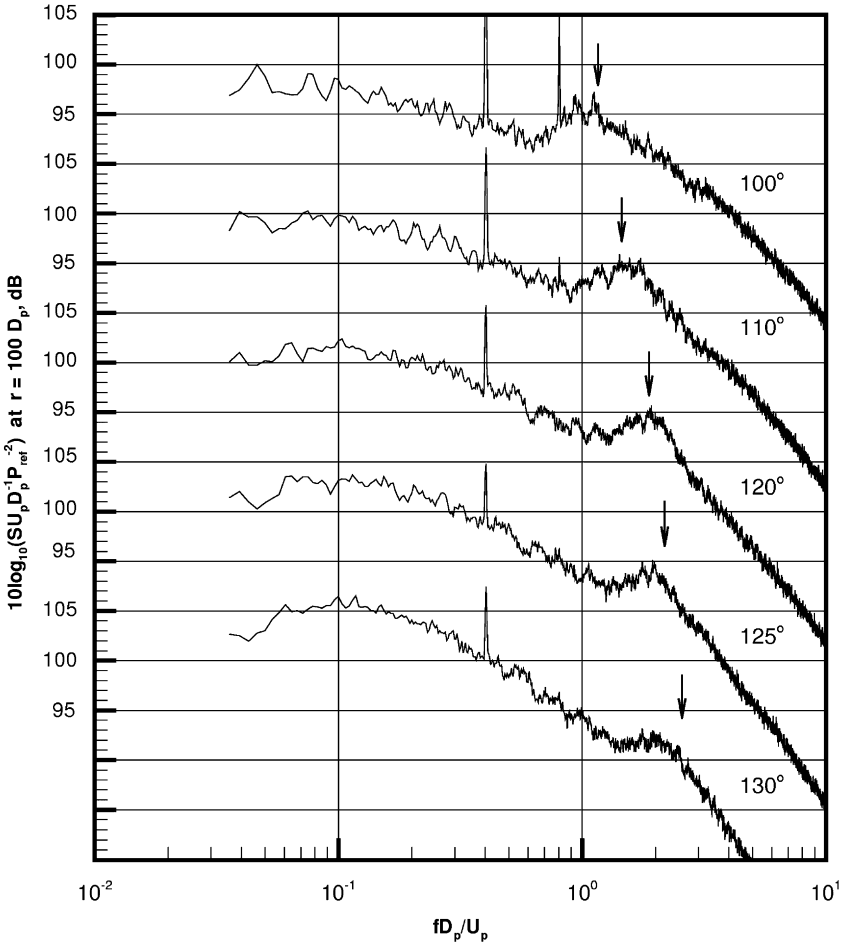

Fig. 30. Comparison of computed and measured peak frequencies of broadband shock-cell noise from a dual stream jet at $M_p = 0.85$, $T_p^{(r)}/T_a = 2.26$, $M_s = 1.28$, $T_s^{(r)}/T_a = 1.0$. Computed peak frequencies are indicated by arrows.

The values of u_{inner} used are $0.94u_p$, $0.835u_p$, and $0.77u_p$, respectively, for the three jets. The agreement between computed peak frequencies and experimental measurements is good. Space limitation does not allow us to show comparisons at other jet operating conditions. We would like to report that the agreement is comparable to those in Figs. 25–30. Based on the good agreement obtained, it is our belief that formula (28) and (60) are valid for broadband shock-cell noise predictions.

6. Conclusion

In this paper, experimental evidence is presented to show that broadband shock-cell noise from a dual stream jet consists of two components. The first component has characteristics very similar to those of single stream supersonic jets. The noise is radiated primarily in the upstream direction and decreases in intensity as inlet angle increases. The second component is new. It radiates mainly in the downstream direction. The noise intensity is low at 90° and increases as inlet angle increases. However, the noise level exhibits a rapid roll-off at larger inlet angles. It is proposed that both noise components are generated by the interaction of large turbulence structures in the shear layers of the jet and the shock-cell structure in the jet plume. The first noise component is generated in the outer mixing layer and the second component is generated in the inner mixing layer.

A vortex sheet dual stream jet model is developed in this investigation to elucidate the noise generation, transmission, and radiation processes. The model provides formulas relating the peak frequencies of

broadband shock-cell noise and direction of radiation for both components. The predictions of these formulas have been compared with experimental measurements and good agreement has been found in all cases. This provides support for the validity of the model. The model solution indicates the existence of a roll-off of broadband shock-cell noise generated in the inner mixing layer as the direction of radiation (inlet angle) becomes large. The physical explanation of the roll-off is that the source responsible for sound radiation to large inlet angle is moving at a subsonic speed relative to the supersonic secondary jets. This causes the disturbances generated to decay exponentially in transmitting through the secondary jet, resulting in significant reduction in radiated noise. This roll-off phenomenon is in full agreement with experimental observations.

One of the main objectives of shock-cell noise research is to develop a noise prediction theory. This is beyond the scope of the present work. However, the model developed in this investigation and the new understanding it provides could serve as the basis for the development of a comprehensive broadband shock-cell noise theory for dual stream jets in the future.

Acknowledgments

The work of CKWT and NNP was supported by a contract from the Boeing Company. Dr. Viswanathan is the Technical Monitor and Boeing Principal Investigator for the project.

Appendix A. The flow of a finite thickness jet over a wavy wall

Consider a uniform flow of velocity u_∞ over a wavy wall as shown in Fig. 31. The wavy wall has a maximum displacement amplitude ε and a wavenumber α. For small ε, the disturbances produced are governed by the linearized momentum and energy equations.

$$\rho_\infty u_\infty \frac{\partial u}{\partial x} = -\frac{\partial p}{\partial x} \tag{A.1}$$

$$\rho_\infty u_\infty \frac{\partial v}{\partial x} = -\frac{\partial p}{\partial y} \tag{A.2}$$

$$u_\infty \frac{\partial p}{\partial x} + \gamma p_\infty \left(\frac{\partial u}{\partial x} + \frac{\partial v}{\partial y}\right) = 0. \tag{A.3}$$

The boundary conditions are

$$y \to \infty, \quad (u, v, p) \text{ are bounded or behave like outgoing disturbances} \tag{A.4}$$

$$y = 0, \quad \frac{v}{u_\infty} = \varepsilon\alpha \cos \alpha x. \tag{A.5}$$

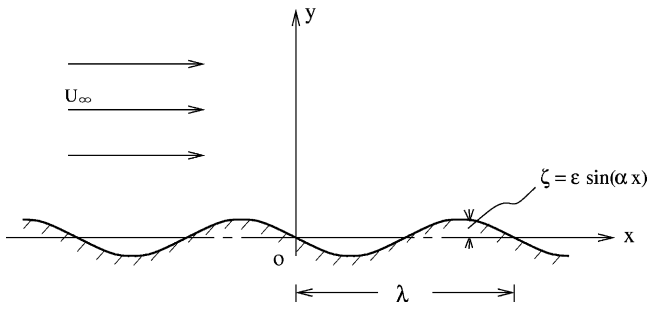

Fig. 31. Uniform flow past a wavy wall of wavelength λ.

By eliminating u and v from Eqs. (A.1)–(A.3), it is easy to find that the governing equation for p is

$$(M_\infty^2 - 1)\frac{\partial^2 p}{\partial x^2} - \frac{\partial^2 p}{\partial y^2} = 0 \tag{A.6}$$

where $M_\infty = u_\infty/a_\infty$, $a_\infty^2 = \gamma p_\infty/\rho_\infty$.

For $M_\infty > 1$ or supersonic flow, the solution of (A.6) that satisfies boundary conditions (A.4) and (A.5) is

$$p = \frac{\rho_\infty u_\infty^2 \alpha\varepsilon}{(M_\infty^2 - 1)^{1/2}} \cos[\alpha(x - (M_\infty^2 - 1)^{1/2} y)]. \tag{A.7}$$

For $M_\infty < 1$ or subsonic flow, the solution is

$$p = -\frac{\rho_\infty u_\infty^2 \alpha\varepsilon}{(1 - M_\infty^2)^{1/2}} \mathrm{e}^{-\alpha(1-M_\infty^2)^{1/2} y} \sin(\alpha x). \tag{A.8}$$

The above solutions indicate that if the relative velocity between the flow and the wavy wall is supersonic, then the disturbances created will pass through the fluid without change in amplitude. However, if the relative velocity is subsonic, then the amplitude of the transmitted disturbances will decay exponentially with increase in distance from the wall. For a fluid layer with finite thickness, the disturbances that reach the other side of the layer is much less intense than that near the wall. Furthermore, for a wavy wall with short wavelength (or higher wavenumber) the intensity of the transmitted acoustic disturbances is much weaker.

References

[1] M. Harper-Bourne, M.J. Fisher, The noise from shockwaves in supersonic jets, *Proceedings of the AGARD Conference on Noise Mechanisms*, AGARD CP-131, Brussels, Belgium, 1973.

[2] J.C. Yu, Investigation of the noise fields of supersonic axisymmetric jet flows, PhD Thesis, Syracuse University, 1971.

[3] H.K. Tanna, An experimental study of jet noise, part 2, shock associated noise, *Journal of Sound and Vibration* 50 (1977) 429–444.

[4] J.M. Seiner, T.D. Norum, Experiments on shock associated noise of supersonic jets, AIAA Paper 79-1526, 1979.

[5] J.M. Seiner, T.D. Norum, Aerodynamic aspects of shock containing jet plumes, AIAA Paper 80-0965, 1980.

[6] C.K.W. Tam, H.K. Tanna, Shock associated noise of supersonic jets from convergent–divergent nozzles, *Journal of Sound and Vibration* 81 (1982) 337–358.

[7] T.D. Norum, J.M. Seiner, Measurements of mean static pressure and far field acoustics of shock-containing supersonic jets, NASA TM 84521, 1982.

[8] T.D. Norum, J.G. Shearin, Effects of simulated forward flight on the structure and noise of an underexpanded jet, NASA TP 2308, 1984.

[9] J.M. Seiner, J.C. Yu, Acoustic near field properties associated with broadband shock noise, *AIAA Journal* 22 (9) (1984) 1207–1215.

[10] T.D. Norum, J.G. Shearin, Shock structure and noise of supersonic jets in simulated flight to Mach 0.4, NASA TP-2785, 1988.

[11] T.D. Norum, M.C. Brown, Simulated high speed flight effects on supersonic jet noise, AIAA Paper 93-4388, 1993.

[12] W.H. Brown, K.K. Ahuja, C.K.W. Tam, High speed flight effects on shock associated noise, AIAA Paper 86-1944, 1986.

[13] C.K.W. Tam, J.M. Seiner, J.C. Yu, Proposed relationship between broadband shock associated noise and screech tones, *Journal of Sound and Vibration* 110 (1986) 309–321.

[14] K. Viswanathan, M.B. Alkislar, M.J. Czech, Characteristics of the shock noise component of jet noise, AIAA Paper 2008-2835, 2008.

[15] C.K.W. Tam, Stochastic model theory of broadband shock associated noise from supersonic jets, *Journal of Sound and Vibration* 116 (1987) 265–302.

[16] C.K.W. Tam, Broadband shock-associated noise of moderately imperfectly expanded supersonic jets, *Journal of Sound and Vibration* 140 (1990) 55–71.

[17] C.K.W. Tam, Broadband shock-associated noise from supersonic jets in flight, *Journal of Sound and Vibration* 151 (1991) 131–147.

[18] C.K.W. Tam, Broadband shock-associated noise from supersonic jets measured by a ground observer, *AIAA Journal* 30 (1992) 2395–2401.

[19] C. Lui, S.K. Lele, Sound generation mechanism of shock-associated noise, AIAA Paper 2003-3315, 2003.

[20] S.K. Lele, Phased array models of shock-cell noise sources, AIAA Paper 2005-2841, 2005.

[21] D.J. Bodony, J. Ryu, S.K. Lele, Investigating broadband shock-associated noise of axisymmetric jet using large eddy simulation, AIAA Paper 2006-2495, 2006.

[22] H.K. Tanna, C.K.W. Tam, W.H. Brown, Shock-associated noise of inverted profile coannular jets: part 1, experiments, part 2, conditions for minimum noise, part 3, shock structures and noise characteristics, *Journal of Sound and Vibration* 98 (1985) 95–145.

[23] D.F. Long, The structure of shock cell noise from supersonic jets, AIAA Paper 2005-2841, 2005.

[24] D.F. Long, Effect of nozzle geometry on turbofan shock cell noise at cruise, AIAA Paper 2005-0998, 2005.

[25] Y.A. Abdelhamid, U.W. Ganz, Prediction of shock-cell structure and noise in dual stream flow nozzles, AIAA Paper 2007-3721, 2007.
[26] C.K.W. Tam, N.N. Pastouchenko, K. Viswanathan, Computation of shock cell structure of dual stream jets for noise prediction, *AIAA Journal* 46 (11) (2008) 2857–2867.
[27] O.H. Rask, E.J. Gutmark, S. Martens, Broadband shock associated noise suppression by chevrons, AIAA Paper 2006-0009, 2006.
[28] O.H. Rask, E.J. Gutmark, S. Martens, Shock cell modification due to chevrons, AIAA Paper 2007-0831, 2007.
[29] E.J. Gutmark, O.H. Rask, U. Michel, How chevrons decrease broadband jet noise in cruise, AIAA Paper 2007-3611, 2007.
[30] D.C. Pack, A note on Prandtl's formula for the wave length of a supersonic gas jet, *Quarterly Journal of Mechanics and Applied Mathematics* 3 (1950) 173–181.
[31] C.K.W. Tam, J.A. Jackson, J.M. Seiner, A multiple-scales model of the shock-cell structure of imperfectly expanded supersonic jets, *Journal of Fluid Mechanics* 153 (1985) 123–149.
[32] C.K.W. Tam, On the noise of a nearly ideally expanded supersonic jet, *Journal of Fluid Mechanics* 51 (1972) 69–95.
[33] K. Viswanathan, Jet aeroacoustic testing: issues and implications, *AIAA Journal* 41 (9) (2003) 1674–1689.
[34] K. Viswanathan, Instrumentation considerations for accurate jet noise measurements, *AIAA Journal* 44 (6) (2006) 1137–1149.
[35] F.D. Shields, H.E. Bass, Atmospheric absorption of high frequency noise and application to fractional-octave band, NASA-CR 2760, 1977.
[36] K. Viswanathan, Parametric study of noise from dual-stream nozzles, *Journal of Fluid Mechanics* 521 (2004) 35–68.
[37] S.C. Crow, F.H. Champagne, Orderly structures in jet turbulence, *Journal of Fluid Mechanics* 48 (1971) 547–591.
[38] G.L. Brown, A. Roshko, On density effects and large structures in turbulent mixing layers, *Journal of Fluid Mechanics* 64 (1974) 775–816.
[39] B. Thurow, M. Samimy, W. Lempert, Compressibility effects on turbulence structures of axisymmetric mixing layers, *Physics of Fluids* 15 (6) (2003) 1755–1765.
[40] C.K.W. Tam, K. Viswanathan, K.K. Ahuja, J. Panda, The sources of jet noise: experimental evidence, *Journal of Fluid Mechanics* 615 (2008) 253–292.
[41] C.K.W. Tam, K.C. Chen, A statistical model of turbulence in two-dimensional mixing layers, *Journal of Fluid Mechanics* 92 (Pt. 2) (1979) 303–326.
[42] C.K.W. Tam, P. Chen, Turbulent mixing noise from supersonic jets, *AIAA Journal* 32 (9) (1994) 1774–1780.